Title

Acoustically Driven Microbubbles Enable Targeted Delivery of microRNA-Loaded Nanoparticles to Spontaneous Hepatocellular Neoplasia in Canines

Journal

Advanced Therapeutics, 3(12)

ISSN

2366-3987

Authors

Kumar, Sukumar Uday
Telichko, Arsenii V
Wang, Huaijun
et al.

Publication Date

2020-12-01

DOI

10.1002/adtp.202000120

Peer reviewed

HHS Public Access

Author manuscript

Adv Ther (Weinh). Author manuscript; available in PMC 2021 December 01.

Published in final edited form as:

Adv Ther (Weinh). 2020 December ; 3(12): . doi:10.1002/adtp.202000120.

Acoustically Driven Microbubbles Enable Targeted Delivery of microRNA-Loaded Nanoparticles to Spontaneous Hepatocellular Neoplasia in Canines

Sukumar Uday Kumar,
Molecular Imaging Program at Stanford (MIPS), Stanford University, Stanford, California; Department of Radiology, Stanford University, Stanford, California

Arsenii V. Telichko,
Molecular Imaging Program at Stanford (MIPS), Stanford University, Stanford, California; Department of Radiology, Stanford University, Stanford, California

Huaijun Wang,
Molecular Imaging Program at Stanford (MIPS), Stanford University, Stanford, California; Department of Radiology, Stanford University, Stanford, California

Dongwoon Hyun,
Molecular Imaging Program at Stanford (MIPS), Stanford University, Stanford, California; Department of Radiology, Stanford University, Stanford, California

jeremy.dahl@stanford.edu, paulmur8@stanford.edu, wculp@ucdavis.edu.

Author contributions: R.P., J.J.D. and W.T.N.C designed the study; R.P. and S.U.K. wrote the manuscript and were involved in synthesis of nanoparticles and ex-vivo tissue analysis; A.T., H.W. and D.H. were involved in ultrasound procedure optimization and treatment, E.G.J., M.S.K., R.B.R. and W.T.N.C were involved in patient recruitment and surgical procedures.

Supporting Information

Figure S1. (a) Gel retardation assay and (b) quantitative plot of free microRNA in spermidine-microRNA polyplexes at different weight ratios; (b) surface zeta potential and (c) electrophoretic measurements of spermidine-microRNA polyplexes. Data are shown as mean ± SD (n = 3).

Figure S2. RNase protection assay for free microRNA, spermidine-microRNA polyplexes and microRNA loaded PLGA-b-PEG nanoparticles.

Figure S3. Surface zeta potential of PLGA-b-PEG nanoparticles, microRNA loaded PLGA-b-PEG nanoparticles and RNase treated microRNA loaded PLGA-b-PEG nanoparticles.

Figure S4. Expression level of target microRNAs in normal liver tissue and HCC in dogs. Data represented as mean ± SD (n = 3). *p≤ 0.05, **p≤ 0.001 and ***p≤ 0.0001.

Figure S5. Quantitative RT-PCR analysis of change in miR-122 (A, C & E) and anti-miR-21 (B, D &F) in different tissues (normal liver, US treated tumor and untreated tumor), blood, and urine samples of dog patients (Dog 1 (A,B), Dog 2 (C,D) and Dog 3 (E,F)) involved in US-MB mediated delivery of miRNA loaded PLGA-b-PEG NPs. All data represented as mean ± SD. Unpaired, two tailed Student's t-test was used for comparison between two groups. *p≤ 0.05, **p≤ 0.001 and ***p≤ 0.0001 p≤ 0.05, **p≤ 0.001 and ***p≤ 0.0001

Figure S6. (A) Immunohistology of CD8+ T cell population in normal liver, untreated liver tumor and US treated liver tumor region of all three dog patients and (Bb) quantitative plot of number of CD8 positive T cells / FOV (n=10) for each dog patient and (a) average number of cells for all three patients. Data represented as mean ± SD. One-way ANOVA with Bonferroni post hoc test was used for statistical significance analysis indicated as *p≤ 0.05, **p≤ 0.001 and ***p≤ 0.0001 p≤ 0.05, **p≤ 0.001, ***p≤ 0.0001 and ns – not significant.

Figure S7. H&E stained sections of (A) Control liver, (B) Untreated Liver tumor and (C) US treated Liver tumor tissue in Dog 1

Figure S8. H&E stained sections of (A) Control liver, (B) Untreated Liver tumor and (C) US treated Liver tumor tissue in Dog 2

Figure S9. H&E stained sections of (A) Control liver, (B) Untreated Liver tumor and (C) US treated Liver tumor tissue in Dog 3

Table S1. Characterization of PLGA-b-PEG nanoparticles for its size, PDI and zeta potential by DLS.

Table S2. Details of the patients recruited for the study.

Table S3. Volume and number of nanoparticles and microbubbles used for delivery in all three patients.

Table S4. Patient blood and urine biochemistry.

Competing interests: The authors do not have any competing interests to declare.

Eric G. Johnson,
Department of Surgical and Radiological Sciences, School of Veterinary Medicine, University of California, Davis, California

Michael S. Kent,
Department of Surgical and Radiological Sciences, School of Veterinary Medicine, University of California, Davis, California

Robert B. Rebhun,
Department of Surgical and Radiological Sciences, School of Veterinary Medicine, University of California, Davis, California

Jeremy J. Dahl,
Molecular Imaging Program at Stanford (MIPS), Stanford University, Stanford, California; Department of Radiology, Stanford University, Stanford, California

William T. N. Culp,
Department of Surgical and Radiological Sciences, School of Veterinary Medicine, University of California, Davis, California

Ramasamy Paulmurugan
Molecular Imaging Program at Stanford (MIPS), Stanford University, Stanford, California; Department of Radiology, Stanford University, Stanford, California

Abstract

Spatially localized microbubble cavitation by ultrasound offers an effective means of altering permeability of natural barriers (i.e. blood vessel and cell membrane) in favor of nanomaterials accumulation in the target site. In this study, a clinically relevant, minimally invasive ultrasound guided therapeutic approach is investigated for targeted delivery of anticancer microRNA loaded PLGA-*b*-PEG nanoparticles to spontaneous hepatocellular neoplasia in a canine model. Quantitative assessment of the delivered microRNAs revealed prominent and consistent increase in miRNAs levels (1.5-to 2.3-fold increase ($p<0.001$)) in ultrasound treated tumor regions compared to untreated control regions. Immunohistology of ultrasound treated tumor tissue presented a clear evidence for higher amount of nanoparticles extravasation from the blood vessels. A distinct pattern of cytokine expression supporting CD8+ T cells mediated “cold-to-hot” tumor transition was evident in all patients. On the outset, proposed platform can enhance delivery of miRNA-loaded nanoparticles to deep seated tumors in large animals to enhance chemotherapy.

Graphical Abstract

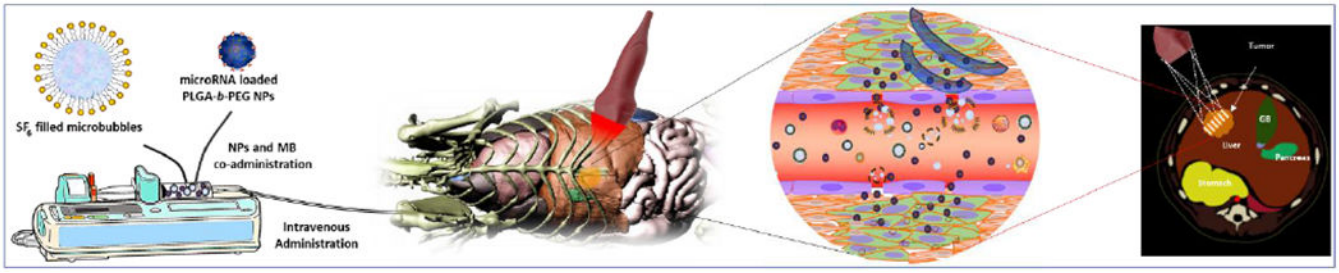

Table of Contents

This work describes a non-invasive means of altering permeability of natural barriers in favor of nanomaterials accumulation in the target tissues by US triggered MB cavitation. Single curvilinear ultrasound array transducer with clinical-grade SonoVue MB enhanced anticancer microRNA loaded PLGA-*b*-PEG NPs delivery by 1.5-to 2.3-folds in canine patients with spontaneously occurring hepatocellular neoplasia

Keywords

focused ultrasound; microRNA; nanoparticles; microbubbles; dog model; targeted delivery; microRNA delivery

1. Introduction

Since the conception of ultrasound (US) in medicine, it has rapidly evolved and emerged as one of most frequently used diagnostic tools in clinical settings, and has found predominant applications in imaging accessible visceral organs, as well as subcutaneous body structures including tendons, muscles, and joints.[1] With the development of microbubble (MB) contrast agents, a new dimension in US imaging has emerged, which extends its application beyond a mere diagnostic imaging tool, to a diverse group of non-invasive imaging-guided therapeutic approaches.[2–4] US contrast agents are gas filled MBs surrounded by a shell made from proteins or phospholipids, which have been clinically used as intra-vascular contrast agents all over the world for over 20 years.[5] The oscillating pressure field induced by US wave impinging upon the MB surface creates stable compressions and expansions of the gas core at lower acoustic pressures (tens to hundreds of kPa) which leads to stable cavitation of MBs.[6–8]

Under high-pressure US waves (up to several MPa), these MBs undergo violent rupturing and dissipate physical force in its vicinity by inertial cavitation. When MBs expand and rupture near endothelial wall, a fluid jet/shock wave is formed followed by an increase in vascular permeability.[9] High pressures can be achieved by focusing ultrasound energy to a tight focal area. Focusing is achieved by applying delays to the US pulses emitted from different elements of a transducer array or by using transducers with a concave shape. Time delays are designed to achieve constructive interference of individual US waves in the desired focal zone with high ultrasound pressures capable of inducing inertial cavitation. [10–12] The regions closer to the transducer or around the focal zone have significantly lower ultrasound induced pressures and are thereby incapable of inducing inertial cavitation to destroy MBs.

In contrast to small molecule drugs, nanoscale materials exhibit passive accumulation in tumor by enhanced permeability and retention (EPR) effect.[13] Although EPR effect is active in the majority of tumors, it is severely limited by the heterogeneous vascularization, differential permeability of vasculature, and highly increased interstitial fluid pressure in the tumor.[14–16] Such inter- and intra-tumoral variance in pathological features of the tumor profoundly hampers nanoparticle accumulation, and distribution in the tumor, leading to

inefficient anti-tumor activity by the delivered therapeutics.[17] A promising solution to tackle such tumor-associated vascular heterogeneity has been sought by increasing the nanoparticles accumulation by US triggered inertial cavitation of MBs in the tumor microenvironment.[18] MB cavitation promotes the formation of fluid microjets, shockwaves, streaming, and cavitation forces, which in turn give rise to shear stresses on the cellular membrane and vascular barrier.[19] These forces breach the blood vessel walls and facilitate extravasation of small molecules and nanoscale materials from the blood stream to the tumor cells.[20] Such forces increase vascular porosity and hence overcome the high variability of the EPR effect.

In this study, we investigated the US-MB mediated targeted delivery of poly-(lactic-co-glycolic) acid copolymer- poly (ethylene glycol) (PLGA-*b*-PEG) NPs loaded with miRNAs which are dysregulated in hepatocellular carcinoma (HCC) (Figure 1). Aberrant expression of miRNAs plays a critical role in tumor initiation, progression, and metastasis.[21] In HCC, miRNA-122 and miRNA-21 have been identified to play pivotal roles in tumor progression, migration, and chemo-resistance.[22] Tumor suppressive miRNA-122 is significantly downregulated in all stages of HCC development.[23] Therefore, therapeutic restoration of miRNA-122 activity has the potential to not only slow HCC growth, but also render these tumors sensitive to chemotherapy. In contrast, miRNA-21 is highly over-expressed in HCC and plays an important role in tumor initiation, progression, and chemoresistance.[24] Therefore, therapeutic silencing of miRNA-21 function using antisense-miR-21 can inhibit HCC cell proliferation, migration, and invasion while also mitigating drug resistance. However, the lack of safe and efficient approaches to deliver miRNAs to the diseased sites hinders clinical translation of miRNA modulation therapy. Intravenously injected miRNAs are rapidly degraded by nucleases and therefore need to be protected to extend their circulation lifetime in the blood. Food and Drug Administration (FDA)-approved biodegradable PLGA-*b*-PEG NP can be used to protect miRNAs from degradation and can be actively delivered into cancer by using therapeutic US with image-guidance, overcoming the limitations of passive tumor accumulation and delivering miRNA deeply into tumors, even in less vascularized portions of the tumor.[25] Recently, our group has optimized the acoustic parameters to maximize PLGA-*b*-PEG NP delivery in human HCC xenografts in mice, and investigated the feasibility of miRNA delivery in deep liver tissue in a pig model.[26] The optimum ultrasound operating parameters used in this study include: acoustic pressure of 5.3 MPa (MI = 3.8; I_{spta} = 26.4 mW/cm^2), pulse repetition frequency of 4 Hz, and duty cycle and number of pulses of 800, required for cavitation of sulfur hexafluoride-filled MBs for nanoparticle delivery.

Although nanomaterials hold promise of an alternative strategy, their clinical evaluation has been constrained to rodent tumor models of allograft or xenograft, which fail to completely mimic clinical scenarios. This pertains to clinical advancement of nanoparticle therapies in patients with hepatocellular carcinoma. Hence, the use of appropriate large animal models of cancer that more closely recapitulate the processes involved in tumor initiation, progression, and pathogenesis in humans, would be a valuable approach.[27] Spontaneous canine tumors of liver are good models for human cancer studies, resulting in their use in biodistribution, pharmacokinetic, and efficacy studies on novel anticancer drugs. Liver tumors constitute ~12.5% of all tumors in dogs, and are usually malignant. Biological, histological, and

genomic features of HCC in humans and dogs are highly similar and have provided a basis to evaluate novel therapeutics in dogs with liver cancer.[28] In addition, the tumor development, phenotype and response to therapy are similar to human HCC.[29, 30]

Thus, given the comparable anatomic size of humans and dogs afflicted with HCC, spontaneous liver tumors of canine may better mirror the therapeutic outcomes in patients with liver cancer. Moreover, mature miRNAs of human and dog possess high sequence homology when compared to many other species, which offers another advantage of replicating the same miRNAs for treatment of HCC in both dogs and humans.[31–33] Given these favorable similarities, translational drug development studies in dogs with HCC have been successfully utilized for investigational therapeutic agents intended for development for clinical application in humans.[34] Herein, we report US-guided MB-mediated delivery of PLGA-*b*-PEG NP loaded with complementary miRNAs (anti-miR-21 and miR-122) to spontaneously occurring hepatocellular neoplasia in dog patients. We show here the US clinical set-up, NP dose, delivery efficiency, and toxicity related to NP treatment in these dogs. The results show that by using this approach, it is feasible to achieve significant level of miRNA loaded NP delivery to treated tumor without any toxicity to the patient. The delivery strategy of miRNAs (miR-122 and anti-miR-21) in this study can be further combined with chemotherapy to improve therapeutic outcomes in dogs with spontaneous HCC, and ultimately translated to patients with HCC.

2. Results and discussion

2.1. Synthesis and characterization of anti-miR-21 and miR-122 co-loaded PLGA-*b*-PEG NPs

PLGA-*b*-PEG NPs co-loaded with anti-miR-21 and miR-122 was formulated using water-in-oil-in-water (w/o/w) double emulsion solvent evaporation method.[35] Given the double emulsion state of nanoparticles, its stability is determined by the stability of two interfaces such as, w/o and o/w. Thus, in order to render interfacial stability to PLGA-*b*-PEG nanoparticles, we used two different emulsifiers such as Tween 80 and Span 80 to stabilize w/o and o/w interfaces, respectively.[36, 37] Spermidine was used as a counterion for electrostatic complexation of miRNAs. The dynamic light scattering (DLS) analysis of as prepared control NPs showed sizes in the range of 166 ± 34 nm with a polydispersity index (PDI) of 0.168 (Figure 2A and Table S1). In contrast, the miRNAs (anti-miR-21 and miR-122) co-loaded NPs showed much lower zeta potential compared to control NPs as a result of loading anionic miRNAs within the nanoparticles (Figure 2B and Table S1). We calculated the entrapment efficiency of loaded miRNAs in the NPs by organic phase extraction followed by densitometric quantification of extracted miRNA after resolved in agarose gels with respect to loaded known standards. The encapsulation efficiency (EE) of 5 different batches of miRNA loaded PLGA-*b*-PEG NPs were estimated, and the results observed the average EE was within the range of 66.8% to 80.4% (Figure 2C). Subsequently, we performed RNase protection assay in order to assess the susceptibility of miRNA loaded within PLGA-*b*-PEG NPs to RNase activity. RNase protection assay revealed that more than 90% of miRNAs loaded within the nanoparticles remained intact, while less than 10% of the miRNAs were intact when a similar quantity of free miRNAs was

treated with RNaseA (Figure 2D). The presence of PEG brushes on the nanoparticle surface as well as the two interfaces (i.e. w/o and o/w) limit the access of RNaseA to miRNAs for digestion, when miRNAs are loaded within the nanoparticles. A small fraction of miRNAs which are exposed on the surface of nanoparticle are prone for RNase activity. In order to assess for the presence of a small fraction microRNA on the surface of the nanoparticles during nanoparticle synthesis, we performed an electrostatic interaction assay where we complexed microRNA with the spermidine, which we used as first emulsion for nanoparticles synthesis, at different N/P ratios (1:1 to 22.5:1). The electrostatic interaction of microRNA with the cationic spermidine neutralizes the proportional negative charge of the phosphate group of microRNAs. The results of gel retardation assay as well as zeta potential measurements of microRNA complexed with spermidine at different N/P ratios are provided in Figure S1 of the revised manuscript. The optimum spermidine-microRNA polyplexes of 25 pmol microRNA with 1 μg spermidine (1:15 -ratio; Figure S1 (A–C)**, Lane 6**) carry a partial negative surface potential (i.e. −8.3 mV) was used for loading in PLGA-*b*-PEG nanoparticles. The gel retardation assay results shown in Figure S1(A) indicates that with the increase in N/P ratio of polyplexes, higher amount of microRNA was entrapped in the polyplex, resulting in gradual decline in free microRNA present in subsequent lanes for up to the ratio of 15:1 (Lane 6). On the basis of this observation, we chose the ratio of 25 pmol microRNA polyplex with 1 μg of spermidine (Lane 6- N/P of 15: 1) as an optimum ratio for electrostatic loading of microRNAs to achieve loading efficiency of ~65-80%. At the same time, interestingly, at higher N/P ratios (i.e. >15, Lane 7 (N/P- 18.75:1) and Lane 8 (N/P-22.5:1)) the extent of microRNA entrapment by spermidine began to decline which led to prominent increase in free microRNA levels. This deviation in trend is expected to be an outcome of alkaline pH manifested by the increasing amount of spermidine in the polyplexes. The net positive charge of spermidine molecule is governed by the protonation of the three amine groups with *pKa* values of 8.25, 9.71, and 10.90 respectively. At alkaline conditions (i.e >pH10) majority of these amine groups are deprotonated leaving net neutral charge in each spermidine molecule. As an outcome of loss of protonated amine groups of spermidines at alkaline conditions the electrostatic interaction with negatively charged microRNA is severely limited in the polyplexes of higher N/P ratio. Such pH dependent shift in cationic nature of spermidine led to the prominent increase in free microRNA levels at higher N/P ratios.[38]

In addition, all polyplexes used for gel retardation assay were also assessed for surface zeta potential measurements by Zetasizer-90 (Malvern Instruments, Worcestershire, United Kingdom). Spermidine as such demonstrated a high positive zeta potential value of +42 mV, whereas microRNA without spermidine loaded in lane 1 possessed a negative zeta potential of −29.1 mV. With increasing weight ratios of spermidine to microRNA, the zeta potential of the polyplex shifted gradually towards positive values. The electrophoretic mobility of the polyplex also declined gradually following the same trend towards higher spermidine to microRNA ratios **(**Figure S1 (C and D**))**. The gradual increase in surface zeta potential indicates that at higher spermidine to microRNA weight ratios, more microRNA is electrostatically encapsulated in polyplex and the remnant small fraction of free microRNA accounts for marginal negative zeta potential. Thus, as it is evident from gel retardation assay as well as surface zeta potential measurements, the polyplexes of spermidine-

microRNA at the N/P ratio of 15:1 tend to have some loosely bound microRNA, which lends negative surface zeta potential of −8.3 mV. In the PLGA-*b*-PEG nanoparticles synthesis procedure some of these polyplexes are impregnated on the surface of the nanoparticles, which contributes to further decline in zeta potential as compared to control PLGA-*b*-PEG nanoparticles without microRNAs. This observation was also validated by gel electrophoresis of microRNA loaded PLGA-*b*-PEG nanoparticles as such **(**Figure S2 (A) (Lane 6)**)**, which revealed that under the influence of electric field small fraction of loaded microRNAs that are loosely bound on the nanoparticle surface are released. We noticed an interesting observation while imaging the electrophoresed microRNA-spermidine polyplex in the gel that the Cy5 fluorescence of free microRNA showed very strong Cy5 signal while we didn't see proportional Cy5 fluorescence from the fraction of microRNA entangled with spermidine and retained in the well itself. It is likely to happen because, spermidine in the polyplex subjects the Cy5 dyes in the proximity to highly alkaline condition, and as a result of which the Cy5 fluorescence is completely quenched.[39]

We used the microRNA-spermidine polyplex of N/P 1:15 for subsequent second emulsion to load into PLGA-*b*-PEG nanoparticles. Some of these polyplexes arrive at the surface of PLGA-*b*-PEG nanoparticles, the competitive interaction of anionic COOH groups with microRNA polyplexes is expected to weaken the microRNA interaction with spermidine to some extent, and thereby exposes the surface microRNA to RNase mediated degradation. To further confirm the presence of microRNA on the surface of nanoparticles and to understand its contribution to the surface charge of the microRNA loaded PLGA-*b*-PEG nanoparticles, we acquired zeta potential of microRNA loaded PLGA-*b*-PEG nanoparticles with and without RNase treatment. As indicated in Figure S3, the zeta potential of RNase treated microRNA loaded nanoparticles increased to −18 mV whereas, the nanoparticle without RNase treatment showed −24 mV as surface potential. The observed increase in value of zeta potential is expected to be an outcome of RNase mediated degradation of negatively charged microRNAs which are present on the surface of the nanoparticles. It is a clear evident from this observation that some microRNAs (~10%) are present on the surface of the nanoparticles and their anionic nature contributes to the surface zeta potential of microRNA loaded PLGA-*b*-PEG nanoparticles.

The susceptibility of microRNA loaded in PLGA-*b*-PEG nanoparticles to RNase action is limited by two different interactions: 1) the electrostatic interaction of microRNA with spermidine and 2) the presence of PEG brushes on the nanoparticle surface. Thus, in order to understand the extent of their contribution to RNase protection effect, we evaluated the stability of microRNA in microRNA–spermidine polyplexes and microRNA loaded PLGA-*b*-PEG nanoparticles to RNase treatment (Figure S2). Although spermidine could protect predominant percentage of microRNA (i.e. 83% Figure S2, Lane 4) from RNase activity for 10 mins, it could not sustain such RNase protection effect at longer incubation time of 30 mins, where only 34% (Lane 5) of the total microRNA was left intact. In contrast to this, microRNA loaded in PLGA-*b*-PEG was observed to be much more stable even at longer incubation time in RNase (71.3% after 30 mins) indicating the crucial role of spongy PLGA core as well as PEG brushes on the surface in limiting the access microRNA for RNase activity. In comparison, microRNA-spermidine polyplexes loaded in PLGA-PEG

nanoparticles could protect nearly 71.3% of loaded microRNA from RNase degradation whereas in the case of microRNA complexed with spermidine only 34% of microRNA could be protected from RNase degradation. It is evident from this observation that if polyplexes were solely attached to the carboxy group in the PEG brush of PLGA-PEG nanoparticle surface, it would not be possible to protect 71.3% microRNA from RNase protection assay. Thus, spermidine microRNA polyplexes are present predominantly within PLGA-PEG nanoparticles rather than on its surface, which is also evident in existing literature.[36, 37] As predominant microRNA-spermidine polyplexes were encapsulated within the PLGA-PEG nanoparticles, in our earlier study, we observed a gradual and sustained release of microRNAs from these nanoparticles over a sustained period of time (i.e. ~8% of microRNA loaded in the nanoparticles was released in 8 days of incubation at 37 °C under a static condition).[35]

In a standard microRNA loaded PLGA-*b*-PEG NPs synthesis procedure, we used 10 mg of PLGA-*b*-PEG polymer along with 10 nmols of miRNAs for each batch of NPs. We suspended the final NPs in 1 mL water and used for further experiments. The concentration of PLGA-*b*-PEG NPs in the final suspension was estimated by Nanoparticle tracking analysis (NTA). The concentration was in the range of $5.97 \times 10^{12} \pm 1.31 \times 10^{12}$ particles/mL (Figure 2E). We further quantified the number of miRNAs loaded within each NPs by qRT-PCR analysis. The results found ~708 ±340 molecules of miRNAs were loaded in each of PLGA-*b*-PEG NPs with the size of 166 ± 34 nm (Table S1).

We estimated the endotoxin levels of each batch of miRNA-loaded PLGA-*b*-PEG NPs using LAL-based chromogenic assay kit. The endotoxin levels were found to be < 0.4 EU mL^{-1}, which is well below the safe limits reported for dogs (the suggested range is 5 EU/kg) considering the nanoparticles dose of 0.1 mL/kg used for treatment (Figure 2F). We used clinically approved SonoVue MB contrast agent (approved in the United States under the name Lumason) for the animal experiments. We reconstituted each vial of SonoVue MB in 5 mL of 0.9% physiological saline and characterized for the MBs size and number using AccuSizer SPOS particle analyzer. The results revealed ~$2.8x10^8$ MBs/mL with the average size of 1.1μm ± 0.85μm (Figure 2G).

2.2. Anti-miR-21 and miR-122 co-loaded PLGA-*b*-PEG NPs uptake in HCC cells

We further evaluated the uptake of synthesized miRNA loaded PLGA-*b*-PEG NPs in HCC cells. We used human liver carcinoma cells (HepG2) for the experiment. We tested the NPs uptake and cellular entry in cells by treating with 5 pmols of Cy5 tagged miRNA loaded NPs (Cy5-anti-miR-21 and miR-122). The cells were treated with NPs for 24 hours and further stained with lysotracker green for lysosome detection and Hoechst 33342 for nucleus tracking, and evaluated the intracellular level of NPs using confocal microscope. Intracellular NPs were observed in the cells as evidenced by the presence of Cy5 fluorescence signal (Figure 2H). Most of the red florescence signal originated from Cy5-tagged miRNA-loaded NPs overlapped with green fluorescence from lysotracker, indicating the endocytosed intracellular state of nanoparticles. Apart from this, the diffused Cy5 fluorescence signal observed throughout the cells depicts free miRNAs released from the nanoparticles. The red fluorescence, green fluorescence, blue fluorescence and bright field

line intensity profile in over a specific segment of (A'---B') of cell presented a clear picture of intracellular PLGA-*b*-PEG NPs speckled with red fluorescent miRNA and its colocalization with green fluorescent endosomes (Figure 2I). Size, surface charge, and coating of NPs have been shown to influence particle–protein interactions at the cell membrane, and determine the events of cellular uptake. The negative electrostatic potential of miRNA nanoparticles, however, excludes the role of electrostatic interaction with the cell membrane (partial negative potential). The presence of dynamic PEG chains on the nanoparticle surface significantly masks its surface charge and, at the same time, its intrinsic ability to solubilize in both polar and nonpolar solvents facilitates its initial integration with the bilayer cell membrane. Thus, based on surface charge and PEG coating on miRNA-loaded PLGA-*b*-PEG nanoparticles, endocytosis and transmembrane transport would be a prevalent mechanism of cellular uptake. Apart from the surface characteristics of nanoparticles, its size distribution in the range of 120–160 nm favors clathrin or caveolin-mediated endocytosis (which is not effective for nanoparticles beyond 200 nm). Overall, unlike rapid cellular uptake of cationic nanoparticles, the miRNA-loaded PLGA-*b*-PEG nanoparticles adapt a slower and controlled uptake phenomenon to avoid nanoparticle associated toxicity.[40]

2.3. Patient recruitment and preparation for the study procedure

Dog patients were recruited by UC Davis veterinary clinic thorough clinical trial recruitment protocol with the owners written consent (IACUC protocol number: 20233). The patients admitted with the disease were screened by abdominal US and CT imaging protocol and the suspected patients were admitted for biopsies. The biopsy samples were submitted for histopathological evaluation to confirm the presence of hepatocellular neoplasia. The details for the three patients enrolled in the study are provided in Table S2. The study included dogs of different weight categories. Although it would be ideal to have dog patients of same body weight, but at the same time it is difficult to recruit patients (dogs) of same breed with similar tumor size for clinical trials especially considering patients with spontaneously developed liver tumors. The dose of miRNA loaded PLGA-*b*-PEG NPs and MBs was normalized with respect to body weight (Table S3). The complete study plan is outlined in the schematics of Figure 3A. The transducer position and orientation for US treatment in each dog patient is depicted in Figure 3B–D.

2.4. Abdominal US and CT Imaging of Tumor topography

Abdominal CT scan (Pre-contrast, vascular-phase and delayed post-contrast CT) of dog 1 revealed a mass within the caudal, ventral aspect of the left liver extending into the left medial liver lobe (Figure 3E). The approximate dimension of the mass identified was 7 x 7.5 x 8.5 cm with minimal arterial supply. The mass had heterogeneous contrast enhancement in venous and delayed phases and multiple small hypoattenuating cavitations. The hepatic lymph nodes were normal. US imaging also presented a similar dimensions of tumor mass i.e. 7.5 x 6 x 4 cm mass in the left liver, effacing the majority of one of the liver lobes. The mass showed a moderately well-defined, and round margin. The liver also featured numerous patchy hyperechoic regions within the mass. The hepatic lymph nodes and other abdominal organs were staged as normal. Preliminary histopathology analysis revealed hepatocellular adenoma.

In dog 2, a large pedunculated liver mass was identified on left lobe of the liver, which was centrally hypoattenuating and peripherally contrast enhancing. The tumor measured approximately 11 x 9 cm as measured in the sagittal plane (Figure 3F). Most notably, the hepatic lymph nodes were enlarged with patterned heterogeneous contrast enhancement and contrast intensity similar to the hepatic mass. Histopathology analysis identified the tumor to be hepatocellular adenoma.

In dog 3, the CT scan revealed a large mass with heterogeneous contrast enhancement in the left aspect of the liver. The approximate dimension of the tumor was 10.2 x 8.0 x 10.2 cm. The axial portion of this mass abutted and depressed the margin of the gallbladder whereas the caudal margins of the liver extended past the costal arch (Figure 3G). This mass led to caudo-dorsal displacement of the stomach. Histopathology analysis identified the tumor to be hepatocellular carcinoma. In each dog patient, US treatment volume was chosen with respect to an arbitrary landmark position (Figure 3H–K), which enabled us to precisely identify and harvest the US treated and untreated tumor tissues during the tumor resection and subsequent analysis. On the basis of tumor topology, appropriate US treatment region were identified at different depths in each dog patient i.e. at 60 mm for dog 1, 50 mm for dog 2 and at 25 mm for dog 3, which turned to be treatment volumes of 6.8 cm^3, 6.3 cm^3 and 3.9 cm^3, respectively. The US treatment region was positioned at different volume and depth of US treatment region. A 3D stereo view of liver lobes and tumor topology in each dog patient is provided in Figure 3L to depict the diversity of location and tumor volume in each patient.

The similarity in pathogenesis, progression, and therapeutic response (pharmacokinetics and metabolism) by spontaneous canine hepatocellular adenoma/carcinoma to that of human HCC serves as a most appropriate pre-clinical model for validating new therapeutic approaches.[41] In order to reinforce this baseline assumption, we investigated the expression level of target miRNAs in dog HCC so as to draw clear correlation with human HCC miRNA epigenetics (Figure S4). Quantitative RT-PCR estimation of miR-122 expression in the dog HCC tissue samples revealed ~83.33% downregulation as compared to that of normal liver tissues. Likewise, in humans, it is well established that there is approximately a 70% reduction in miR-122 expression in HCC as compared to that of normal tissue.[29] Since miR-122 expression level is consistently downregulated in HCC, it has been identified as a clinically relevant biomarker for staging and predicting the survival of human patients with HCC.[42] It controls neoplastic transformation by altering HOTAIR/miR-122/Cyclin G1 negative regulatory axis.[43] Therapeutic strategies aimed at re-expressing miR-122 have resulted in inhibition of tumor growth, and has been shown to enhance sorafenib-induced apoptosis, which led us to the rationale behind delivery of miR-122 in this study.[44] Apart from miR-122, we also measured miR-21 and miR-16 expression in normal liver and neoplastic tissues from the dogs, as they also have a similar expression profile in human HCC. In contrast to miR-122, miR-21 expression in general is upregulated in most solid tumors including human HCC. We observed significant upregulation of miR-21 expression in dog liver neoplasia tissues, which is again in close agreement to that of human HCC. miR-21 is reported to be an oncomiR that repress the expression of a range of tumor suppressor genes related to metastasis, proliferation, apoptosis and drug resistance.[45] Treatment with anti–miR-21, is a well-established strategy for functional inactivation of

endogenous miR-21, which effectively leads to induction of caspase activity, apoptosis, and necrosis in HCC cells. In our earlier studies, we have established that a combination of miR-122 and anti-miR21 is the most potent combination for inflicting antiproliferative effects in HCC and sensitization to doxorubicin treatment.[46, 47] Likewise, miR-16 downregulation in human HCC resulted in suppression of proliferative activity and inhibition of invasion and metastasis.[48] Quantitative estimation of miR-16 in dog HCC also revealed similar downregulation (~5 folds) as compared to normal liver. Beyond these epigenetic and pathological similarity of spontaneous liver neoplasia of dog to human HCC, the similarity in physiological and anatomical aspects of liver favors the feasibility of focused US orientation and operating parameters. US-mediated targeted MB destruction has been previously used for gene delivery into canine livers; one such study involved an invasive procedure (injection of pDNA/MB complexes into a portal vein segmental branch) accompanied by US for delivery of pDNA into liver lobes.[49] In another study, a sonosensitizer, epirubicin loaded micelles (NC-6300) (Size - 60–70 nm) were used in combination with HIFU for treatment of hepatocellular carcinoma in spontaneous HCC dog patients.[50] To the best of our knowledge, this is the first study which investigates of US-MB assisted targeted delivery of miRNA-loaded PLGA-*b*-PEG nanoparticles to spontaneous hepatocellular neoplasia in canine model.

2.5. Quantitative *ex vivo* evaluation of miRNA loaded PLGA-*b*-PEG nanoparticles delivery by US

The maximum administered intravenous dose of miRNA-loaded PLGA-*b*-PEG NPs was 0.1mL/kg of animal weight, i.e. 5.97×10^{11} NPs/kg of animal body weight. Similarly, reconstituted SonoVue MB were administered at ~ 1.4×10^{8} MB/kg of animal body weight. Clinically, 2 to 2.4 mL (6×10^{8}) of reconstituted MB is typically administered for an adult human patient for contrast enhanced US scan of the liver. This dose can be repeated if needed for up to 4.8 mL in human patient.[51] The dogs were anesthetized and intubated during the delivery procedure. The dogs breathing frequency, heart rate, oxygen saturation (SpO2), mean arterial blood pressure were monitored based on area under Receiver-operating characteristics (ROC) curve, and maintained within the range of 0.90 – 0.95. We injected MB and NP co-suspension by intravenous infusion over the course of a 40 min time period. Histology and blood work (Table S4) did not indicate any instance of neutropenia, cardiomyopathy, or any anaphylactic reaction. The PEGylation (stealth NPs) improves the stability and circulation time by increasing water solubility, which reduces renal clearance and improving “passive” targeting to tumors.[52] It provides long plasma residence time and decrease uptake by reticuloendothelial system (RES). Until now, among the nanopharmaceuticals available on the market, only liposomal doxorubicin (Doxil/Caelyx, Myocet) has been tested in a canine model to assess its pharmacokinetics, biodistribution, and safety.[53] Recent reports have suggested that in dog models, repeated doses of PEGylated NPs instigates Anti-PEG IgG response, resulting in a loss in efficacy with subsequent doses.[54] Because this study is intended to deliver nanoparticles by US to the extravascular tumor cells, the antibody response to PEG from previous doses may not be problematic in further delivery doses by this approach.

Quantification of miRNAs in the tissue, blood and urine followed a consistent pattern in all three dogs. In each case, the US treated tumor tissue had a much higher quantity of delivered miRNA as compared to the untreated liver tumor tissue or the normal liver tissue itself. The extent of miRNA delivery was quantified in terms of both anti-miR-21 and miR-122 (Figure 4). Quantitative plot of the absolute value of expression levels of samples is presented in Figure S5, where we observed that the trend in expression levels of respective microRNAs was consistent with the normalized plot. Apart from miR-122 delivered by the NPs to the tumor tissues, the cells themselves have endogenous baseline expression of miR-122 which obscures precise quantitation of delivered miR-122, which is further compounded by the fact that we do not have pre-treatment tissue equivalents to eliminate basal miR-122 expression levels in corresponding tissues. In spite of endogenous miR-122 presence in the tissues, the trend in miRNA delivery was consistent with that of anti-miR-21, i.e. US treated liver tissue had much higher levels of miR-122 as compared to non-treated liver tumor tissue or the normal liver tissue. The only difference between the two was that anti-miR-21, being endogenously absent, manifested a much higher fold change in delivery as compared to miR-122 with respect to pre-treatment control samples. Quantitatively, in the case of the Australian Shepherd (dog 1), an approximate 1.52×10^6 ($\pm 4.79 \times 10^5$) fold increase in anti-miR-21 was observed in the US treated region, whereas only an approximate 2.93×10^5 ($\pm 3.2 \times 10^4$) fold increase in anti-miR-21 level was observed in the untreated tumor of the same lobe (normalized with respect to anti-miR-21 quantified in skin) (Figure 4B). Thus, we observed a strong 5-fold ($p<0.001$) increase in delivery of anti-miR21 as a result of focused US treatment in the tumor tissue. The level of miRNA in the normal liver was also quantified to determine the extent of off-target delivery, which was found to be nearly 4 folds lower for anti-miR-21 in liver compared to the US treated tumor tissue. Since liver tends to be a clearance organ for nanoparticles, and macrophages tend to phagocytose nanoparticles and home into liver, hence the background accumulation is naturally expected to be high in the normal liver.[55] Quantitative estimation of miR-122 also well correlated with that of anti-miR-21; the US treated tumor tissue was 430 ±14 fold higher, whereas untreated tumor tissue and normal liver tissue were 110 ±18 and 245 ±27 fold higher, respectively, compared to signals in the skin (Figure 4A). The quantitative fold change in delivered miRNA were normalized with respect to GAPDH. Apart from the liver tissues, significant levels of both the miRNAs were also detected in blood and urine samples collected 24 hours after NPs administration, which clearly indicates prolonged circulation time of PEGylated NPs in the blood stream, and also support the stability of loaded miRNAs in the nanoparticles, even in the urine where the pH is very high. As an outcome of such prolonged circulation-time of nanoparticles, they continue to accumulate passively in the tumor tissue.

In spite of diverse attributes of the 3 canine patients, the miRNA delivery levels were consistent across all dogs with no delivery associated toxic effect, which ascertains the promising implication of this therapeutic procedure to diverse hepatic neoplasia patients (Figure 4). Quantitatively estimation of miRNA revealed that in case of dog 2, 4.97×10^7 ($\pm 3.9 \times 10^5$) folds of anti-miR21 were delivered to the US treated tumor region whereas untreated tumor mass and normal liver tissue had 3.27×10^7 ($\pm 9 \times 10^5$) and 2.47×10^7 ($\pm 5 \times 10^5$) folds, respectively compared to skin (Figure 4D). In terms of miR-122, the US treated

region had 470-fold higher miR-122 levels (includes both endogenous and delivered miR-122) as compared to 280-fold higher levels in untreated region when compared to that of skin (Figure 4C). The strong correlation of the differences in delivered miRNA and US treatment is a clear evidence of MB-US assisted enhanced delivery of miRNA loaded PLGA-*b*-PEG NPs in the target region of tumor tissue. A spider plot of microRNAs (anti-miR-21 and miR-122) in normal liver tissue, untreated tumor tissue and US treated tumor tissue clearly illustrated skewed distribution of delivered micro RNA towards US treated tumor tissue in all dog patients (Figure 4, G and H).

Acoustic cavitation of MBs by focused US has previously been used for delivery of drugs and nucleic acids (pDNA, mRNA and micoRNA) in large animal pre-clinical models.[56] Although US guided delivery of drug loaded MB has entered clinical trials for treatment of pancreatic and liver cancer, delivery of therapeutic nucleic acids still remain under-explored.[57] Comparative oncologists consider dogs as the closest model to humans for pre-clinical evaluation of cancer therapeutics. Liu *et al.*, used focused US in combination with MBs as vectors for cardiac transfection of miR-21 in pigs.[58] Similarly, Dewitte *et al.*, delivered mRNA to lymph nodes in dogs through destruction of MBs.[59] In both studies, they used nucleic acid loaded in the MBs itself, the extent of delivery can be severely limited by the stability of nucleic acids because of their exposure to nucleases. In addition, the acoustic sheer stress in MBs can impair the stability of nucleic acid payload. Moreover, due to the short circulation time and life span of MBs *in vivo*, off target delivery is inevitable. In order to overcome aforementioned drawbacks, in the present work we have adopted PLGA-*b*-PEG nanocarriers for loading miRNA and enhanced their inherent EPR accumulation in tumor by MB cavitation in the tumor milieu. The miRNA-loaded nanoparticles not only lend access to sub-micron leaky tumor vasculature of the tumor but also has a long circulation time *in vivo*, which enables cumulative accumulation of nanoparticles in the tumor over the course of time.

2.8. Analysis of urine and blood biochemistry

The complete blood count, serum biochemistry profiles, and urine analysis were performed in all three patients 24 hours after US-MB delivery PLGA-b-PEG NPs treatment (Table S4). No evidence of hypersensitivity, pain or gastrointestinal toxicity was observed in any of the patients with current dose of nanoparticles and MBs used for delivery, or from the US treatment pulses used for treatment. During subsequent follow-up period, the injection sites were unremarkable, and no systemic signs of toxicity were noticed (e.g. weight loss, loss of appetite, or abnormal behavior). No dog displayed clinical signs of hematologic, hepatic or renal toxicity. Blood biochemistry revealed elevated levels of serum alkaline phosphatase, alanine amino transferase, aspartate amino transferase, and lactic dehydrogenase in all 3 patients indicating liver dysfunction. Two of the dog patients (dog 2 and dog 3) were on lower margins of hypoglycemic state as a result of HCC triggered insulin-like growth factor type II (IGF) production.[60] Low red blood cell counts with low hemoglobin values were also observed. Overall, liver function tests were abnormal in almost all dogs. Two patients (i.e. dog 1 and dog 2) presented a case of hypercholesterolemia as an outcome of increased cholesterol incorporation in plasma lipoproteins by diseased liver.[61]

2.9. Immune cytokine profile in blood and urine samples

US targeted MB destruction by itself can instigate cytokine storms and modulate the tumor immune microenvironment. Such immunostimulatory cytokine storms have the potential to switch the nonimmunogenic “cold tumor” (associated with immunosuppressive TAM) to “hot tumor” by recruitment of cancer-fighting T cells.[62] The transition from cold-to-hot tumor is characterized by signs of inflammation, and in order to assess if US-MB therapy manifests such effects, we quantified the expression levels of some important regulatory inflammatory cytokine markers including Interleukin-1 beta (IL-1β), Myeloid differentiation factor 88 (MYD 88), Interleukin-6 (IL-6), Interleukin-6 (IL-12), Tumor Necrosis Factor alpha (TNF-α), and Interferon gamma (IFN-γ), in blood and urine samples of dog patients before and after US-MB-miRNA-NP treatment. The quantitative analysis revealed that although no significant change in expression of IL-12, IL-6 or IFN-γ were observed, a drastic increase in expression of IL-1β, MYD 88 and TNF-α was observed consistently in the blood samples of all three patients (Figure 5A). Elevated cytokines and persistent inflammation establish a hallmark microenvironment for “cold-to-hot” tumor transition by recruiting macrophages, dendritic cells, natural killer cells, and T and B lymphocytes.

Interleukin-1 beta (IL-1β) belongs to IL-1 family of pro-inflammatory cytokines which plays an essential role in injury and inflammation. IL-1β is identified as a marker for the detection of early stages of inflammation when leukocytosis does not yet appear in peripheral blood. Nonetheless, the possible use in diagnosis is restricted due to the fact that usually only low amounts of IL-1β to be detected in the serum. In contrast to this, in the present study we observed a prominent increase in expression IL-1β in the blood. IL-1β is one of the most important inflammatory cytokines. IL-1β precipitates acute attacks of both local and systemic inflammation. Besides TNF-α, IL-1β is one of the first pro-inflammatory cytokines increasing in inflammation, which is important because every cytokine plays a precise role in regulating the expression of other cytokines. TNF-α mRNA expression levels in peripheral blood leukocytes are well known to increase by ~2-5 folds in cancer bearing patients. In the present study, given the pre-condition of hepatic neoplasia in dog patients, the TNF-α expression in peripheral blood leukocytes was higher, but surprisingly after US treatment and miRNA delivery, a drastic increase in expression (~16-21 fold ($p<0.001$)) of TNF-α was observed. This observation is consistent with our earlier study, where we reported that US targeted MB destruction in HCC mouse xenografts triggered a 189±33% increase in TNF-α (in 0.5 h post treatment).[63] Since TNF-α is an inflammatory cytokine predominantly secreted by activated leukocytes in blood stream, and it is plausible that the observed surge in TNF-α is an outcome of US-MB treatment mediated recruitment and activation of leucocytes in HCC. The recruitment of tumor infiltrating leukocytes (T lymphocyte) in the tumor milieu primes the switch from “cold” HCC tumor into “hot” tumor augment therapeutic miRNA combination therapy against HCC. One mechanism in this vital transition is generating tumor-reactive T lymphocyte with the capacity to resist tumor associated myeloid-derived suppressor cells (MDSC). A recent report suggests that MyD88-activated CD8+ T cells i.e. MDSC is essential to overcome this barrier.[64] The MyD88 protein serves as an adaptor molecule in Toll-like receptor signaling pathway required for activation of tumor infiltrating CD8+ T cells. Quantitative assessment of MyD88 expression levels in dog patients before and after US-MB and miRNA treatment indicated a prominent

95-150-fold ($p<0.001$) increase in expression level in the blood which supports its plausible role in overcoming immunosuppressive tumor microenvironment by activation of tumor infiltering CD8+ T cells. Furthermore, in line with this hypothesis, we investigated presence of tumor infiltrating CD8+ T cells in normal liver, untreated liver tumor, and US treated liver tumor tissue by immunohistochemistry (Figure 5, B and D and S6). The number of CD8+ T cells in the field of view (n=10 slices for each dog) was quantified for each treatment conditions in all three dog patients, and values were plotted as average number of CD8+ T cells/field of view (Figure S6). The analysis revealed a significant increase in the number of CD8+ T cells in US treated tumor (~8.1 CD+ T cells/FOV) as compared to normal liver tissues (~4.3 CD8+ T cells/FOV) ($p<0.001$). On the other hand, we also observed significantly higher number of CD8+ T cells in untreated tumor tissues (~7.4 CD8+ T cells/FOV) (Figure S6, C). It is evident from these results that US treatment triggered infiltration of CD8+ T cells not only to treated tumor tissue but also to untreated tumor tissues. It is possible that tumor specific antigens released from ultrasound treated tumor region are recognized by the immune system, which subsequently elicits tumor specific CD8+ T cell recruitment. As these tumor specific CD8+T cells are trained against tumor specific antigens they do not distinguish between US treated and untreated tumor tissue, and as a result of this we did not observe significant difference in CD8+ T cell population between US treated and untreated tumor tissues.[65] In broad perspective gained by microscopic observation, it was evident that normal liver tissue had much lower CD8+ T cells as compared to that of tumor tissues (untreated and US treated). Although higher number of CD8+ T cells were found in the tumor tissue there was insignificant difference between untreated and US treated tumor tissues. Although immunohistology results complement well with the hypothesized correlation of immune cytokine profile further quantitative immunoassays are essential for drawing concluding remarks. However, the results outlined here lead to a potential therapeutic outcomes of US triggered immunomodulation in the tumor microenvironment.

It is evident that US-MB mediated delivery of miRNA-loaded PLGA-*b*-PEG nanoparticle triggers inflammatory markers involved in protumor to antitumor immunity transition. Thus, evaluation of the therapeutic significance of such anti-tumor immune response to potentiate the miRNA combination therapy warrants a longitudinal dog study with complete dose-response characteristics. Apart from this, the study also presents a successful strategy for targeted delivery of miRNA loaded PLGA-*b*-PEG nanoparticles to spontaneously occurring liver tumors, which opens the potential for therapeutic implications in a future longitudinal study in combination with chemotherapy.

2.10. Histopathology of hepatic tumors

We also performed H&E staining of control and US treated tumor tissues to observe the cavitation-induced bio-effects. The examination of stained histology section of ultrasound treated tissue did not present any instance of detectable tissue damage or intra- and peri-tumoral hemorrhage (Figure 5, E to J). The intact endothelial lining of blood vessels in the US treated region also corroborates well with safe US operating parameters for clinical translation in drug/nanoparticle delivery applications. The tumor pathology of each patient revealed diverse characteristics (Figure S7 to S9). Most of the neoplasms had a wide trabecular (>3 cells) pattern characterized by narrow or broad cylindrical masses or

trabeculae that had no significant connective tissue stroma; cytologic atypia, mitotic activity and with an absence of Kupffer cells. There was wide variation in cell morphology, from almost normal appearing hepatocytes to large, polyhedral, spindle, giant and syncytial cells. The nuclei were also pleomorphic, and had thick nuclear margins with prominent nucleoli. A few cells with vacuolated cytoplasm and nuclei were seen. Giant cells, seen occasionally in other groups, were a common feature of this pleomorphic group of neoplasms, and were characterized as large hepatocytes with large or multilobed nuclei, or large, multinucleated cells containing up to 50 nuclei. Bile was found in most of these neoplasms in the canaliculi, but rarely in the cytoplasm of the hepatocytes. Areas of mild nodular regenerative hyperplasia (NRH) and pigment-laden macrophages (lipogranulomas) were also prevalent in all patients.

US triggered MB cavitation extravasates NPs across the blood vessels into the tumor tissue The present study rallies on the rational that US triggered MB oscillation along the walls of blood vessel manifests cavitation-induced acoustic microstreaming, shear stress and shock waves which creates transient gaps or distend the vessel wall to enhance vascular permeability and facilitate PLGA-*b*-PEG NPs to enter into the tumor tissue. In an attempt to trace evidence of such phenomenon we evaluated the untreated and US treated tumor tissues by immunostaining for CD31+ endothelial marker and Anti-PEG antibody. The immunofluorescence images of untreated and US treated tumor regions are shown in Figure 6A. In the case of tumor regions with no US exposure, although significant number of nanoparticles were evident within the blood vessel, a very small fraction of these NPs extravasated from the blood vessel into the tumor tissue. On the other hand, evaluation of blood vessels in ultrasound treated region of the tumor clearly presented evidence of large number of NPs permeating across the blood vessel into the extracellular space. Apart from presenting evidence of extravasated nanoparticles in the proximity of blood vessels, the overall concentration of nanoparticles in US treated tumor tissue was much higher than the untreated tumor tissue. The stark contrast in nanoparticle distribution in these two cases further established that US triggered MB cavitation in the tumor tissue increases the permeation of nanoparticles from the blood vessels, which directly accounts for the observed increase in the delivery of miRNAs. Intensity profile map for fluorescence channels corresponding to CD-31, Anti-PEG and Phalloidin-Red across the cross-section of blood vessels indicates the presence of nanoparticles in the intravascular blood pool and also illustrates the distance of NPs extravasation across the endothelial lining of the blood vessel (Figure 6, B and C). The gradual decline in extravascular nanoparticles with increasing distance from the blood vessel indicates that as the driving thrust of cavitation force declines with distance from the blood vessel. We also observed a decline in concentration of NPs over the given span of extravascular space. Overall, the immunostaining results confirmed the effect of US-MB mediated cavitation in improving the delivery of PLGA-b-PES NPs to the tumor tissues.

3. Conclusion

A new era of cancer therapy has emerged with clinical translation of first-generation nanomedicine that started from Doxil (liposomal doxorubicin in 1995) and expanded to Onivyde (liposomal irinotecan in 2015). Nanoparticles selectively extravasate and

accumulate in tumor as a result of EPR effect where leaky tumor vasculature and non-functional lymphatics facilitate this process. Despite this favorable attribute, heterogeneous EPR effect in tumors, poor vascularization, high interstitial fluid pressure, high tumor cell density, and dense ECM, results in heterogeneous delivery effect with inconsistent therapeutic outcome, which have deterred further developments in the field of nanomedicine. Ultrasound in combination with MB offer a non-invasive strategy to overcome these barriers and revive the scope of nanotherapeutics in medicine. Ultrasound in the presence of MB can trigger non-destructive widening of intercellular spaces between epithelial cells and increase the rate of effective diffusion nanotherapeutics through the tissues while facilitating for increase the penetration of nanoparticles across endothelial junctions. Our research group has shown the effect of this strategy for delivering microRNA loaded PLGA-PEG nanoparticles by combining with ultrasound triggered MB cavitation in tumor xenograft mice models, [46, 47, 56] and established promising therapeutic implications.

Clinical translation of such US based therapeutic approaches to large animals and humans have raised doubts considering ultrasound susceptibility to attenuation and reflection due to tissue viscoelasticity and inhomogeneity, especially with increasing depth of target. The present study addresses this vital gap by using a single curvilinear transducer driven by a research scanner at optimized operating parameter for targeted delivery of anticancer microRNAs (anti-miR-21 and miR-122) loaded NPs in large animals (canine) with spontaneous hepatic neoplasia (Figure 3). To further build on the clinical relevance of this work, we used FDA approved PLGA-*b*-PEG polymer based nanocarrier along with commercial clinical grade MB for imaging guided targeted delivery of microRNA (Figure 2). Quantitative estimation of delivered miRNAs revealed that US treated liver tumor showed ~2 - 5 folds ($p<0.001$) higher anti-miR-21 delivery than the untreated tumor or control normal liver tissues. The consistent pattern in delivered miRNAs levels (US treated tumor region > untreated tumor region) ($p<0.001$) establishes a strong evidence for the versatile noninvasive delivery approach (Figure 4). As human HCC oncogenesis, pathology and genetics is similar to canine, and the mature miRNAs are replicas of human, the results obtained from the current study are highly translatable to human patients with HCC.

On the other hand, histological evidence of increased extravasation of nanoparticles from blood vessels into interstitial tumor tissue in US treated region as compared to that of untreated tumor region corroborated well with microRNA quantitation results (Figure 6). A consistent pattern of elevated cytokines accompanied by increased prevalence of CD8+ T cell in US treated tumor tissue hints to a hallmark signaling cascade for “cold-to-hot” tumor transition. In one of our recent work, we reported such immunomodulatory effects in mouse xenograft HCC tumor treated with similar strategy[63] (Figure 5). With growing evidence along this line, exploiting antitumoral immune effects could enhance the therapeutic efficacy of the proposed combination therapy for HCC. Overall, this study lays the foundation for the safety and efficacy of US guided precise delivery of nanoparticles in dog patients with representative anatomical similarity to humans (in terms of liver size and location) which allows for a smooth transition of this approach to human clinical trials.

4. Experimental Section

Materials:

All chemical reagents used for the study were of analytical grades or above. CellLight® Early Endosomes-GFP, BacMam 2.0 Marker was purchased from Thermo Fisher (Waltham, MA, USA). Primers for various PCR reactions were custom synthesized by PAN Facility at Stanford, at purity above 90%. Antisense-miRNA-21 and miR-122 with more than 95% purities were custom synthesized by PAN Facility at Stanford. Cell culture media and plastic wares for cell culture and nanoparticle synthesis were purchased from BD Biosciences (Sparks, MD). The RNA extraction kit (mirVana™ miRNA Isolation Kit), with phenol, and Reverse Transcriptase kit were purchased from Thermo Fisher (Waltham, MA, USA). Carboxy terminal Poly (lactic-co-glycolic) acid - poly (ethylene glycol) conjugate (PLGA-*b*-PEG) polymer was purchased from Poly SciTech (West Lafayette, IN, USA). ToxinSensorTM Chromogenic LAL Endotoxin Assay Kit was purchased from Genscript (Piscataway, NJ, USA). FDA approved US contrast agent SonoVue® with the commercial name Lumason® was purchased from Bracco Imaging (Milan, Italy). The primary antibodies and IgG anti-rabbit secondary antibody were acquired from Cell Signaling Technology (Danvers, MA, USA). HepG2 (Human hepatocellular carcinoma) cell lines were purchased from American Type Culture Collection (Manassas, VA, USA) and cultured as per ATCC guidelines.

Formulation of anti-miR-21 and miR-122 Loaded PLGA-b-PEG NPs:

PLGA-*b*-PEG nanoparticles loaded with miRNAs/spermidine were formulated by double emulsion solvent evaporation technique with minor modifications [35, 46]. In all co-encapsulation studies, we used 95% antisense-miR-21 and 5% Cy5-antisense-miR-21 along with miR-122 to maintain the consistency of formulation across different experiments for cell culture evaluations, and 100% miR-122 and anti-miR-21 combinations for *in vivo* dog patient studies. miRNAs of 10 nmols (5 nmols each of anti-miR-21 and miR-122) were complexed with spermidine in an N/P ratio of 15:1 at room temperature for 15 min in DNase/RNase free water. The miRNA-spermidine complex was added dropwise to the stirred solution of PLGA-*b*-PEG polymer (10 mg) dissolved in dichloromethane (1 mL) containing 3% Span-80, followed by sonication (VCX 750 Sonicator) for 60 s at 40% amplitude in ice bath to form the first emulsion. To this primary emulsion, 5 mL of emulsifying water (Tween-80, 1% w/v) was added and sonicated at 40% amplitude in ice bath for 60 s to form second emulsion, followed by stirring for 3 h to allow the dichloromethane to evaporate. The NPs were sterile filtered using a 0.45 μm syringe filter (Whatman PURADISC 25 AS, PES, GE Healthcare), and excess surfactants and free miRNAs were removed by an ultrafiltration device with 100 kDa molecular weight cut-off (MWCO) Membrane (Millipore, USA) by centrifuging at 3000 rpm. The washing steps were repeated four times using DNase/RNase free water for complete removal of surfactant before being used for further studies. The concentrated nanoparticles were diluted to a known volume in sterile water, estimated for their particle size, Zeta potential and the loaded miRNAs levels, prior to use in different experiments.

Gel retardation assay for spermidine-microRNA polyplexes:

We determined the optimum N/P ratio for spermidine/microRNA polyplexes by gel retardation assay of the polyplexes prepared at different weight ratios. Spermidine dissolved in RNase free water at 0.1 mg/mL concentration was complexed in different ratios (0.1, 0.25, 0.5, 0.75, 1, 1.25 and 1.5 μg) with 25 pmol of Cy5-microRNA to form polyplexes of different N/P ratios (1:1, 1.5:1, 3.75:1, 7.5:1, 11.25:1, 15:1, 18.75:1, and 22.5:1). The polyplexes were incubated at 37 °C for 15 minutes and then subjected to electrophoresis in 3% agarose gel by running at 60 volts for 30 min. The gel was imaged using IVIS Lumina II system (Caliper Life Science, Hopkinton, MA) imaging system with excitation at 605 nm and emission collected in Cy5 window. The fluorescence signal from Cy5 fluorophore tagged microRNA was quantified as average radiance.

RNaseA protection assay:

RNase protection for spermidine-microRNA polyplexes at optimized N/P ratio was performed to evaluate the susceptibility of microRNA entrapped in the polyplexes to degradation by RNaseA. Spermidine-microRNA (50 pmol) polyplexes (N/P – 15:1) were incubated with RNase (2 μg/ mL) for 10 mins and 30 mins. After the incubation period, 0.2% sodium dodecyl sulfate in 10 μL of DEPC water was supplemented to the polyplexes to stop RNase activity and release microRNAs from spermidine. The samples were loaded in 3% agarose gel and resolved at 60V for 30 mins. Total microRNA extracted from the 50 pmol microRNA complexed with spermidine was used as control for comparison. Likewise, RNaseA protection assay for microRNA loaded PLGA-*b*-PEG nanoparticles was also performed to draw comparison with spermidine-microRNA polyplexes. After incubating microRNA loaded PLGA-*b*-PEG nanoparticles in the presence of RNase for 30 mins the microRNA was extracted from the nanoparticles by DCM assisted solubilization of PLGA-*b*-PEG polymer and phase separation. The extracted microRNA was then subjected to electrophoresis in 3% agarose gel by running at 60 volts for 30 min. The gel was imaged using IVIS Lumina II system (Caliper Life Science, Hopkinton, MA) imaging system with excitation at 605 nm and emission collected in Cy5 window. The fluorescence signal from Cy5 fluorophore tagged microRNA was quantified as average radiance.

Evaluation of miRNAs loaded PLGA-b-PEG nanoformulation for Endotoxin Levels:

Genscript ToxinSensor™ Chromogenic LAL Endotoxin Assay Kit designed to use as a quantitative *in vitro* end-point endotoxin test for human and animal parenteral drugs, biological products, and medical devices, was used for the evaluation of endotoxin levels in nanoparticles prepared in this study. This method utilizes a modified Limulus Amebocyte Lysate and a synthetic color producing substrate to detect endotoxin chromogenically. The kit has a minimum endotoxin detection limit of 0.01 EU/ml and a measurable concentration range of 0.01 to 1 EU/ml. We used 50 μL of miRNA-loaded PLGA-*b*-PEG nanoparticles for Endotoxin assay and quantified endotoxin levels with respect to endotoxin standards provided in the kit.

Particle size and zeta-potential measurements:

Particle size and zeta potential of PLGA-*b*-PEG NPs were measured using a Zetasizer-90 (Malvern Instruments, Worcestershire, United Kingdom). Size measurement was performed at 25°C at a 90° scattering angle. The mean hydrodynamic diameter was determined by cumulant analysis. Zeta-potential measurements were performed using an aqueous dip cell in an automatic mode by Smoluchowski model.

Entrapment efficiency determinations for miR-122 and antisense-miR-21 in PLGA-b-PEG NPs:

The loading and encapsulation efficiency of miR-122 and antisense-miR-21 were evaluated by measuring the entrapped miRNAs in NPs as determined by using organic/aqueous extraction method reported previously with minor modifications.[35] Briefly, known volume of lyophilized NPs was dissolved in 500 μL of dichloromethane (DCM) with a brief vortexing followed by sonication and maintaining the sample at 37 °C for 30 mins. The loaded miRNAs were extracted from the organic (DCM) phase by the addition of 500 μL of TE buffer (10 mM Tris-HCl, 1 mM EDTA, pH 7.4) by vortexing vigorously for 1 min and centrifuging at 12,000 rpm for 5 min at 4°C; aqueous phase was separated, and the extraction procedure was repeated twice to completely extract all the RNAs present within the nanoparticles. All the aqueous phases were combined and the isolated miR-122 and antisense-miR-21 were further tested for their intact size, and independent quantification for each miRNA by gel electrophoresis and RT-PCR. The samples were resolved in 3% agarose gel by running at 60 volts for 30 minutes and imaged by IVIS Lumina II system (Caliper Life Science, Hopkinton, MA) imaging system with excitation at 605 nm and emission collected in Cy 5 window. The fluorescence signal from Cy5 fluorophore tagged microRNA was quantified as average radiance.

In vitro cell uptake analysis of miR-122 and antisense-miR-21 loaded PLGA-b-PEG NPs:

To study the cellular uptake of miRNA loaded nanoparticles, the HepG2 cells were seeded on UV sterilized glass cover slips placed in a 6-well plate, at a density of 50,000 cells/well, and allowed to attach and grow overnight at 37°C in an incubator with 5% CO_2. The cells were treated with 5 pmol of Cy5 tagged miRNA loaded PLGA-*b*-PEG nanoparticles and incubated for 24 hours. At the end of the incubation period, 12 μL of Cell Light Early Endosomes-GFP reagent was added to each well and gently rocked and incubated further for 16 h. After the incubation period, the spent media was aspirated, and the coverslips were gently rinsed with PBS. The nuclei were stained with Hoechst 33258 and then fixed with 4% glutaraldehyde for 2 min and rinsed with PBS before mounting on the glass slide with Fluor Mounting Medium (Trevigen, Gaithersburg, MD). The cells were imaged under a Leica TCS SP8 confocal microscope under red (Ex-640, Em-668), green (Ex- 488, Em-510), and blue (Ex-405, Em-461) filters.

Patient recruitment, screening and preparation for study procedure:

All dog patients were enrolled in the study based on certain inclusion and exclusion criteria. The inclusion criteria included confirmed (cytologic or histopathologic) hepatocellular neoplasia that is amenable to surgical resection with a minimal tumor size of 2 cm and

adequate blood work to establish the safety parameters for undergoing anesthesia and surgery. The patient exclusion criteria were framed as lack of tumor resectability and any instance of abdominal effusion. All the dog patients were pre-screened with an abdominal US and contrast enhanced abdominal computed tomography (CT), and were identified to meet the inclusion criteria. The study population comprised of 3 client-owned dogs from the patient population presenting to the Veterinary Medical Teaching Hospital at the University of California-Davis. The protocol, consent form, and procedures were all per approved by the UC Davis IACUC and the UC Davis Veterinary Medical Teaching Hospital Clinical Trials Review Boards (IACUC protocol number: 20233). The patients' ages and body weights ranged from 11 to 13 years and 6.2 to 30 kg, respectively. Of the 3 dogs, 2 were female and 1 was male. Informed consent for miRNA US therapeutic procedure was acquired from companion owners of each dog patient undergoing tumor resection. Each dog was screened for histologic type of tumor, the anatomic location of the tumor and the clinical status of the dog. These included, but not limited to, physical examination, complete blood count (CBC), serum bio-chemical analysis, urinalysis, and radiographic studies. Eligible dogs were enrolled in the study provided they had adequate hematologic and serum biochemical parameters to undergo procedural steps of US guided delivery of miRNA loaded PLGA-*b*-PEG NPs to the hepatocellular carcinoma, and were free of complicating concurrent disease. Dogs entered had not received chemotherapy within 2 weeks prior to initiation of study, nor was other concurrent therapy being utilized.

Therapeutic US parameters for targeted delivery:

The implemented platform for targeted delivery of miRNA-loaded NPs to deep tissues in large animal models is schematically depicted in Figure 1. MBs and NPs were co-administered intravenously, and MB cavitation was induced by the focused US beam to increase the vascular permeability in the targeted region and facilitates transport of NPs out of the vascular compartment, where the miRNA cargo is released into the parenchyma. The image-guided miRNA delivery was performed using a Vantage 256 research scanner (Verasonics Inc., Redmond, WA, USA) with a single, curvilinear array transducer (C5-2v; Verasonics). The therapeutic ultrasound sequence was similar to those described in our recent work.[26] Briefly, the probe was fixed in a custom 3-D printed holder that is mounted on a jointed flex-arm stand (Dino-Lite MS-52B; AnMo Electronics Corp., Taipei, Taiwan), which is freely rotatable over 360°. The positioning system enables stable and precise accurate probe fixation to the desired target location by locking the arm joints after the targeted portion of liver was identified on the B-mode images. The custom holder allows for rotation of the probe in the out-of-plane direction at angular increments of 2.5°. A B-mode imaging sequence consisting of 40 unfocused plane wave emissions steered between ± 9° with a center frequency of 4.6 MHz was used for image guidance. The resulting B-mode images were displayed with a dynamic range of 60 dB at a frame rate of 6 frames/s. The mechanical index (MI) of the B-mode emissions was 0.05 to avoid nonspecific destruction of bubbles from the imaging pulses. Therapy was delivered using a focused beam with an F-number of 1.2, a center frequency of 2 MHz with 6 cycles and PRF of 4 Hz. A total number of 11 therapy regions focused next to each other with lateral spacing of therapy beam's full-width at half-maximum (FWHM) were applied. After that, the therapeutic plane was rotated for 2.5° to achieve mRNA delivery in elevation dimension. The treatment was performed

sequentially across 10 different planes covering the tumor mass in the liver of approximately 20 × 20 × 27.5 mm^3. For each therapy region, eight hundred pulses were delivered, resulting in a therapy time of 200 sec at 4 Hz PRF. The emitted acoustic pressure was measured with a focus at 70 mm using a needle hydrophone (HNC-0500; Onda, Sunnyvale, CA, USA) in degassed water. The FWHM was 1.9, 2.9, and 21.8 mm in the lateral, elevation, and axial directions, respectively. For calibration, the peak negative pressure was measured with increasing excitation voltage and de-rated with an attenuation factor of 0.5 dB/(cm MHz). The therapeutic US pulse used for miRNA delivery had a derated *in-situ* peak negative pressure of 5.3 MPa (MI = 3.8; Ispta = 26.4 mW/cm^2), based on our previous study in a pig model of liver delivery. [11]

MBs for Delivery:

Clinically approved SonoVue contrast agent (approved in the United States under the name Lumason) was used for all the phantom and *in vivo* experiments. The agent consists of MBs made of a stabilized sulfur hexafluoride gas core surrounded by a phospholipid monolayer shell, with a mean diameter range of 1.5 to 2.5μm. One vial of MBs was resuspended in 5 ml of sterile normal saline and activated to get MB suspension with a concentration of ~2.8 - 5.6 $x10^8$ MBs/mL.

US-guided MB-mediated targeted in vivo delivery of miRNAs loaded PLGA-b-PEG NPs to spontaneous HCC in dog model:

In vivo US-guided targeted delivery of miRNA-loaded PLGA-*b*-PEG nanoparticle delivery was performed in three different patients (Figure 1). The animals were anesthetized using anesthesia protocols determined by the Clinical Anesthesiology Faculty at UC Davis Veterinary Medical Teaching Hospital. The patients were intubated, and anesthesia was maintained with isoflurane (2-4%) in oxygen. Prior to the therapy procedure, the liver and tumor were imaged from a subcostal view. Easily accessible regions were identified in the tumor mass at a depth of approximately 25-60 mm, and the two imaging windows were marked on the skin. Precautions were taken to avoid proximity to gall bladder, stomach and kidney while spanning the transducer across 10 treatment planes. The SonoVue (Lumason) MBs were activated and their dosage was kept consistent at 0.6 mL/kg of body weight. Suspension of PLGA-*b*-PEG NPs co-loaded with antisense-miR-21 and miR-122 (5 ml; 8 × 10^{11} NP/ml) were used at 0.12 ml/kg of body weight. MBs and NPs were mixed with normal saline to ensure the infusion rate at 1.2 ml of mixed solution/kg of body weight for all the patients. A solution of PLGA-*b*-PEG NPs co-loaded with antisense-miR-21 and miR-122 (5 ml; 8 × 10^{11} NP/ml) were mixed with a volume of 5 ml SonoVue (2.8-5.6 $x10^8$ MB/mL), and was diluted with sterile 0.9% physiological saline to a final volume of 30 ml solution (The volume, NP and MB numbers were adjusted based on body weight of the patient). The MB/NP homogenous suspension in normal saline was infused intravenously at a constant rate using a syringe pump (Medfusion 3500; Smiths Medical, Dublin, OH, USA) for the entire duration of the therapy procedure (approximately 35 min). Focused US treatment was initiated 2 min after the MB infusion to ensure a steady state of MB perfusion. The treatment was performed sequentially across 10 different planes covering the tumor mass in the liver.

Surgical procedure and tissue collection:

Blood and urine samples for pharmacokinetic evaluation of the miRNA were drawn before nanoparticle infusion and 24 hours after infusion. Similarly, four milliliters of blood samples were drawn into an EDTA-containing vacutainer tube (Becton Dickinson Vacutainer Systems, Franklin Lakes, NJ) before and 24 hours after the nanoparticles treatment, and the tube was immediately placed on ice. The collected blood and urine samples were stored at −80° C until analysis. After 24 hours, each dog underwent an exploratory laparotomy. The entire liver tumor was resected and samples of the tissues with and without US treatment were obtained for ex vivo analysis. Tissue samples collected for RNA extraction were immediately frozen in liquid nitrogen and stored at −80° C until time of analysis to determine miRNA levels. Complications associated with surgery/recovery were documented. The red blood cell count was monitored following surgery to ensure that no postoperative hemorrhage occurred. Injectable pain medications were administered until the morning of anticipated discharge from the hospital in order to keep the patient comfortable.

Ex vivo miRNAs quantifications from surgical tissue, urine and blood samples:

Different regions of the liver tissues (tumors with treated and untreated areas, and normal liver tissues), blood (pre- and post- treatment), and urine (pre- and post- treatment) samples collected from each patient and snap-frozen on dry ice immediately after collection were processed for miRNA quantification. In case of paraffin embedded tissue samples, xylene was used as solvent to deparaffinize the samples by brief rinse for 3 mins at 50°C. The remnant xylene was removed from the samples by two rounds of 100% ethanol wash, and then air dried before lysing in lysis buffer. Subsequent steps of RNA isolation were followed as per other sample processing procedure. The levels of delivered therapeutic anti-miR-21 and miR-122 were evaluated by qRT-PCR. Tissue samples of 100 mg were homogenized using a PRO250 tissue homogenizer (PRO Scientific, Oxford, CT, USA) using a sterile tip in 300 μl lysis buffer for 3 min. Total RNA (messenger RNA and miRNA) was isolated from the lysates using mirVana miRNA Isolation Kit (Life Technologies, Grand Island, NY, USA) adapting the total RNA extraction procedure according to the manufacturer's protocol. For miRNA quantification, 50 ng of total RNA was reverse transcribed using RT-primers (Life Technologies) specific for anti-miR-21 and miR-122 using a custom ordered TaqMan kit and a miRNA Reverse Transcription Kit (Life Technologies). For GAPDH housekeeping gene and cytokine genes, we used random primer-based cDNA synthesis protocol as mentioned below. qRT-PCR was performed using cDNA (5 ng equivalent of total RNA) combined with TaqMan RT-PCR reagents (primer and probe mix) of anti-miR-21 and miR-122. qRT-PCR was performed by 2 min incubation at 50 °C followed by activation of the DNA polymerase at 95 °C for 10 min, with 40 cycles of 95 °C for 15 s, and 60 °C for 60 s in a Bio-Rad CFX96 Touch™ Real-Time PCR Detection System (Bio-Rad, Hercules, CA). The level of anti-miR-21 and miR-122 was calculated using the $2^{-\Delta\Delta CT}$ method. The qRT-PCR quantification was repeated three times for each analyzed sample. The miRNA levels were normalized to the endogenous level of GAPDH RNA using TaqMan probe, which was administered neither NPs nor US and MB therapy and served as a control.

Cytokines expressions by qRT-PCR:

Whole blood from each dog patient was collected before treatment and 24 h post-treatment in commercially available EDTA-treated tubes and stored at −20 C until processed for total RNA extraction. A consistent volume of 300 μL of whole blood was aliquoted for RNA extraction and homogenized in 300 μL of cell lysis buffer for 3 min. Total RNA was extracted with mirVana™ miRNA Isolation Kit and eluted in 20 μL of DEPC treated dd H_2O. 50 ng of total RNA template was used for cDNA synthesis using random primers and qScript cDNA Supermix Reverse Transcriptase master mix (Quanta Bio). The resulting cDNA transcripts of 5ng RNA equivalent were set up for independent gene specific TaqMan RT-PCR reaction with primer-probe mix designed for IL-12, IL-6 or IFN-γ, IL-1β, MYD 88, GAPDH and TNF-α. The results were normalized with respect to GAPDH and represented as fold change in expression.

Immunofluorescence staining:

The OCT embedded frozen tumor tissues were sectioned into 5 μm thick slices by cryomicrotome. The cryostat temperature was set between −15 and −23 °C and adjusted to achieve isothermal state with the sample. The sections were then air dried for 30 minutes at room temperature to adhere to the slides. Added 50 μL of ice-cold fixation buffer to each tissue section and allowed to fix for 8 minutes at 2-8 °C in a humidifying chamber. The sections were rinsed 3 times with PBS to remove the OCT and fixative solution, and rehydrated with wash buffer for 10 minutes. The sections were then incubated in blocking buffer (1% horse serum in PBST for 30 min at room temperature. To study the delivery profile of the nanocarrier, confirm extravasation of the nanocarrier from the blood vessels into the tumor parenchyma, quantitative immunofluorescence analysis was performed on tissue sections stained for both the vascular endothelial cell marker CD31 and the cytoskeleton F-actin marker. The slices were stained for CD31(Anti-CD31 Antibody FITC), PEG (Anti-PEG antibody) and F-actin (Phalloidin Red). The slides were then incubated in primary antibodies diluted in incubation buffer at 2-8 °C overnight. This incubation regime allows for optimal specific binding of antibodies to tissue targets and reduces non-specific background staining. After the incubation period, the slides were washed 3 times for 15 minutes in wash buffer. Anti-Mouse Cy5 secondary antibody was used to label primary Anti-PEG-Ab. Unlike *in vitro* experiments, fluorescent dye Cy5 tagged microRNA could not be used for dog treatment as they are not clinically approved fluorescent dyes and thus raise additional toxicity concerns. Thus, in sight of such safety concerns and plausible unintended side effects of Cy5, non-fluorescent microRNAs loaded in PLGA-*b*-PEG was tracked by anti-PEG antibody which has already been reported for such purposes in earlier studies. Moreover, absence of PEG in vivo, presents it as most sensitive marker with minimal background to detect the nanoparticles. The slides were then incubated with secondary antibody at room temperature for 30-60 minutes. The slides were washed 3 times for 15 minutes each in wash buffer. Each slide was supplemented with 300 μL of the diluted DAPI solution and incubated for 5 minutes at room temperature. The excess dye was rinsed by washing 2 times with PBS and then mounted with an anti-fade mounting media for visualizing under the confocal fluorescence microscope. Tissue slices were imaged with a Leica TCS SP8 confocal microscope under red (Ex-640, Em-668), green (Ex- 488, Em-510), and blue (Ex-405, Em-461) filters at 40X magnification. Images of the NPs, CD31, and F-

actin were captured in separate color channels (excitation/emission wavelengths were Cy5 (633/670), FITC (488/525) and Phalloidin Red (514/609 nm) respectively).

Hematoxylin and eosin staining:

After 24 h of nanoparticle administration tumor tissues were excised by lobectomy and processed for *ex vivo* histological analysis. Excised tissues were fixed in 4% paraformaldehyde overnight at 4 °C and immersed in 70% ethanol, and then embedded in paraffin, sliced at 5 μm thickness in a Leica microtome (Leica RM2255). Sections were stained in undiluted hematoxylin (Sigma-Aldrich, USA) for 2 min, rinsed in running water, and differentiated in 1% HCl acid/alcohol for 30 s. They were then washed and immersed in bluing solution (Fisher, USA) for 1 min, washed in running water and rinsed in 10 dips of 95% alcohol. After this, slides were counterstained in eosin by dipping into 1:5 ethanol diluted eosin solution (Fisher) for a total of less than 30 s, dehydrated through 95% alcohol, absolute alcohol, and xylene for 5 min each. Slides were mounted with xylene based mounting medium (Permount, Sigma-Aldrich, USA) and imaged using a Nanozoomer (Hamamatsu, Japan).

Statistical Analyses:

Statistical Analyses: GraphPad Prism 8 (version 8.0a; GraphPad Software, Inc., La Jolla, CA) was used to plot all graphs and perform statistical analyses. Data was pooled from 2-10 independent experiments and represented as mean ± standard deviation (SD) or standard errors means (SEM) as indicated, interquartile range between the first (25th percentile) and third (75 percentile) was adopted for analysis. Grouped data were compared using two-tailed Students t-test and multiple comparisons of grouped data were calculated using two-way ANOVA with Tukey's post hoc to determine the significance of difference. One-way ANOVA with Bonferroni post hoc test was also used to draw significance of certain comparisons as indicated. Adjusted p values were considered statistically significant if p values <0.05 and the symbols indicating statistical significance were as follows - *$p \leq 0.05$, **$p \leq 0.001$ and ***$p \leq 0.0001$

Supplementary Material

Refer to Web version on PubMed Central for supplementary material.

Acknowledgements

General: The authors would like to thank Canary Center at Stanford, Department of Radiology for providing the facility and resources for executing this work. We also thank support staff at Department of Surgical and Radiological Sciences at University of California for their kind assistance in treatment procedures. The authors would also like to thank Stanford Animal Histology Services for preparation of histology. We acknowledge Dr. José G. Vilches-Moure, Veterinary pathologist, Animal Histology Services (AHS), for his advice regarding histological analysis of animal tissues. We dedicate this work in memory of Dr. Sanjiv Sam Gambhir and Dr. Juergen K. Willmann.

Funding: This work was supported by the Focused Ultrasound Foundation and the National Institutes of Health (grants numbers R01CA209888, R21EB022298). The authors would like to thank NIH for the funding support for the purchase of Celigo S Imaging Cytometer (200-BFFL-S) used in this study under NIH Small Instrumentation grant [Award No: S10 OD023518-01A1 to RP].

References

[1]. Carovac A; Smajlovic F; Junuzovic D, Acta Inform Medl 2011l, 19 (3), 168–71.

[2]. Ambika Rajendran M, Cureusl 2018l, 10 (9), e3256.

[3]. Chen Y; Liang Y; Jiang P; Li F; Yu B; Yan F, ACS Appl Mater Interfacesl 2019l, 11 (45), 41842–41852.

[4]. Tzu-Yin W; Wilson KE; Machtaler S; Willmann JK, Curr Pharm Biotechnoll 2013l, 14 (8), 743–52.

[5]. Paefgen V; Doleschel D; Kiessling F, Front Pharmacoll 2015l, 6, 197.

[6]. Chen X; Wang J; Pacella JJ; Villanueva FS, Ultrasound Med Bioll 2016l, 42 (2), 528–538.

[7]. Ferrara K; Pollard R; Borden M, Annu Rev Biomed Engl 2007l, 9, 415–47.

[8]. Kogan P; Gessner RC; Dayton PA, Bubble Sci Eng Technoll 2010l, 2 (1), 3–8.

[9]. Collis J; Manasseh R; Liovic P; Tho P; Ooi A; Petkovic-Duran K; Zhu Y, Ultrasonicsl 2010l, 50 (2), 273–9.

[10]. Landini L; Santarelli F; Pomata F; Verrazzani L, J Biomed Engl 1991l, 13 (6), 469–72.

[11]. Xiao Z; Guo Y; Geng L; Wu J; Zhang F; Wang W; Liu Y, Sensors (Basel)l 2019l, 19 (10).

[12]. Hynynen K; Jones RM, Phys Med Bioll 2016l, 61 (17), R206–48.

[13]. Bazak R; Houri M; Achy SE; Hussein W; Refaat T, Mol Clin Oncoll 2014l, 2 (6), 904–908.

[14]. Golombek SK; May JN; Theek B; Appold L; Drude N; Kiessling F; Lammers T, Adv Drug Deliv Revl 2018l, 130, 17–38.

[15]. Yokoi K; Chan D; Kojic M; Milosevic M; Engler D; Matsunami R; Tanei T; Saito Y; Ferrari M; Ziemys A, J Control Releasel 2015l, 217, 293–9.

[16]. Dhaliwal A; Zheng G, Theranosticsl 2019l, 9 (26), 8091–8108.

[17]. Zhang YR; Lin R; Li HJ; He WL; Du JZ; Wang J, Wiley Interdiscip Rev Nanomed Nanobiotechnoll 2019l, 11 (1), e1519.

[18]. Duan L; Yang L; Jin J; Yang F; Liu D; Hu K; Wang Q; Yue Y; Gu N, Theranosticsl 2020l, 10 (2), 462–483.

[19]. Fan Z; Kumon RE; Deng CX, Ther Delivl 2014l, 5 (4), 467–86.

[20]. Yemane PT; Aslund AKO; Snipstad S; Bjorkoy A; Grendstad K; Berg S; Morch Y; Torp SH; Hansen R; Davies CL, Ultrasound Med Bioll 2019l, 45 (11), 3028–3041.

[21]. Kim J; Yao F; Xiao Z; Sun Y; Ma L, Cancer Metastasis Revl 2018l, 37 (1), 5–15.

[22]. Figueiredo M; Esenaliev R, J Drug Delivl 2012l, 2012, 767839.

[23]. Zhu Z; Zhang X; Wang G; Zheng H, Hepat Monl 2014l, 14 (8), e18672.

[24]. Zhu Q; Wang Z; Hu Y; Li J; Li X; Zhou L; Huang Y, Oncol Repl 2012l, 27 (5), 1660–8.

[25]. Lu JM; Wang X; Marin-Muller C; Wang H; Lin PH; Yao Q; Chen C, Expert Rev Mol Diagnl 2009l, 9 (4), 325–41.

[26]. Di Ianni T; Bose RJC; Sukumar UK; Bachawal S; Wang H; Telichko A; Herickhoff C; Robinson E; Baker S; Vilches-Moure JG; Felt SA; Gambhir SS; Paulmurugan R; Dahl JD, J Control Releasel 2019l, 309, 1–10.

[27]. Overgaard NH; Fan TM; Schachtschneider KM; Principe DR; Schook LB; Jungersen G, ILAR Jl 2018l, 59 (3), 247–262.

[28]. Santos NP; Colaco AA; Oliveira PA, Tumour Bioll 2017l, 39 (3), 1010428317695923.

[29]. Ciaputa R; Bandoch P; Lewandowska K; Madej JA; Kandefer-Gola M; Janus I; Nowak M, Veterinarni Medicinal 2016l, 61 (10), 546–552.

[30]. Boomkens SY; Spee B; Ijzer J; Kisjes R; Egberink HF; van den Ingh TS; Rothuizen J; Penning LC, Comp Hepatoll 2004l, 3 (1), 9.

[31]. Zhou D; Li S; Wen J; Gong X; Xu L; Luo Y, Comput Biol Cheml 2008l, 32 (1), 60–65.

[32]. Wagner S; Willenbrock S; Nolte I; Murua Escobar H, Front Genetl 2013l, 4, 46.

[33]. Sahabi K; Selvarajah GT; Abdullah R; Cheah YK; Tan GC, J Vet Scil 2018l, 19 (2), 162–171.

[34]. Khanna C; London C; Vail D; Mazcko C; Hirschfeld S, Clin Cancer Resl 2009l, 15 (18), 5671–7.

[35]. Devulapally R; Sekar NM; Sekar TV; Foygel K; Massoud TF; Willmann JK; Paulmurugan R, ACS Nanol 2015l, 9 (3), 2290–302.

[36]. Oster CG; Kissel T, J Microencapsull 2005l, 22 (3), 235–44.

[37]. Passerini N; Craig DQ, J Control Releasel 2001l, 73 (1), 111–5.

[38]. Gimsa J; Wysotzki P; Perutkova S; Weihe T; Elter P; Marszalek P; Kralj-Iglic V; Muller T; Iglic A, Langmuirl 2018l, 34 (8), 2725–2733.

[39]. Cooper ME; Gregory S; Adie E; Kalinka S, Journal of Fluorescencel 2002l, 12, 425–469.

[40]. Behzadi S; Serpooshan V; Tao W; Hamaly MA; Alkawareek MY; Dreaden EC; Brown D; Alkilany AM; Farokhzad OC; Mahmoudi M, Chem Soc Revl 2017l, 46 (14), 4218–4244.

[41]. Thamm DH, Front Oncoll 2019l, 9, 1257.

[42]. Zhang Y; Li Y; Jiang W; Li Q; Lan Y, Medicine (Baltimore)l 2019l, 98 (13), e14810.

[43]. Fu X; Calin GA, EBioMedicinel 2018l, 37, 17–18.

[44]. Braconi C; Henry JC; Kogure T; Schmittgen T; Patel T, Semin Oncoll 2011l, 38 (6), 752–63.

[45]. Buscaglia LE; Li Y, Chin J Cancerl 2011l, 30 (6), 371–80.

[46]. Chowdhury SM; Lee T; Bachawal SV; Devulapally R; Abou-Elkacem L; Yeung TA; Wischhusen J; Tian L; Dahl J; Paulmurugan R; Willmann JK, J Control Releasel 2018l, 281, 19–28.

[47]. Mullick Chowdhury S; Wang TY; Bachawal S; Devulapally R; Choe JW; Abou Elkacem L; Yakub BK; Wang DS; Tian L; Paulmurugan R; Willmann JK, J Control Releasel 2016l, 238, 272–280.

[48]. Wu WL; Wang WY; Yao WQ; Li GD, Int J Mol Medl 2015l, 36 (6), 1713–9.

[49]. Noble ML; Kuhr CS; Graves SS; Loeb KR; Sun SS; Keilman GW; Morrison KP; Paun M; Storb RF; Miao CH, Mol Therl 2013l, 21 (9), 1687–94.

[50]. Horise Y; Maeda M; Konishi Y; Okamoto J; Ikuta S; Okamoto Y; Ishii H; Yoshizawa S; Umemura S; Ueyama T; Tamano S; Sofuni A; Takemae K; Masamune K; Iseki H; Nishiyama N; Kataoka K; Muragaki Y, Front Pharmacoll 2019l, 10, 545.

[51]. Dietrich CF; Averkiou M; Nielsen MB; Barr RG; Burns PN; Calliada F; Cantisani V; Choi B; Chammas MC; Clevert DA; Claudon M; Correas JM; Cui XW; Cosgrove D; D'Onofrio M; Dong Y; Eisenbrey J; Fontanilla T; Gilja OH; Ignee A, et al., Ultrasound Int Openl 2018l, 4 (1), E2–E15.

[52]. Suk JS; Xu Q; Kim N; Hanes J; Ensign LM, Adv Drug Deliv Revl 2016l, 99 (Pt A), 28–51.

[53]. Zabielska-Koczywas K; Lechowski R, Moleculesl 2017l, 22 (12).

[54]. Hoang Thi TT; Pilkington EH; Nguyen DH; Lee JS; Park KD; Truong NP, Polymers (Basel)l 2020l, 12 (2).

[55]. Gustafson HH; Holt-Casper D; Grainger DW; Ghandehari H, Nano Todayl 2015l, 10 (4), 487–510.

[56]. Wang TY; Choe JW; Pu K; Devulapally R; Bachawal S; Machtaler S; Chowdhury SM; Luong R; Tian L; Khuri-Yakub B; Rao J; Paulmurugan R; Willmann JK, J Control Releasel 2015l, 203, 99–108.

[57]. Mullick Chowdhury S; Lee T; Willmann JK, Ultrasonographyl 2017l, 36 (3), 171–184.

[58]. Qian L; Thapa B; Hong J; Zhang Y; Zhu M; Chu M; Yao J; Xu D, J Thorac Disl 2018l, 10 (2), 1099–1111.

[59]. Dewitte H; Vanderperren K; Haers H; Stock E; Duchateau L; Hesta M; Saunders JH; De Smedt SC; Lentacker I, Theranosticsl 2015l, 5 (1), 97–109.

[60]. Zini E; Glaus TM; Minuto F; Arvigo M; Hauser B; Reusch CE, J Vet Intern Medl 2007l, 21 (1), 193–5.

[61]. Carr BI; Giannelli G; Guerra V; Giannini EG; Farinati F; Rapaccini GL; Marco MD; Zoli M; Caturelli E; Masotto A; Virdone R; Sacco R; Trevisani F, Int J Biol Markersl 2018l, 33 (4), 423–431.

[62]. Popovic A; Jaffee EM; Zaidi N, J Clin Investl 2018l, 128 (8), 3209–3218.

[63]. Wischhusen JC; Chowdhury SM; Lee T; Wang H; Bachawal S; Devulapally R; Afjei R; Sukumar UK; Paulmurugan R, J Control Releasel 2020l, 321, 272–284.

[64]. Parker KH; Beury DW; Ostrand-Rosenberg S, Adv Cancer Resl 2015l, 128, 95–139.

[65]. Westwood JA; Haynes NM; Sharkey J; McLaughlin N; Pegram HJ; Schwendener RA; Smyth MJ; Darcy PK; Kershaw MH, Clin Cancer Resl 2009l, 15 (24), 7624–7633.

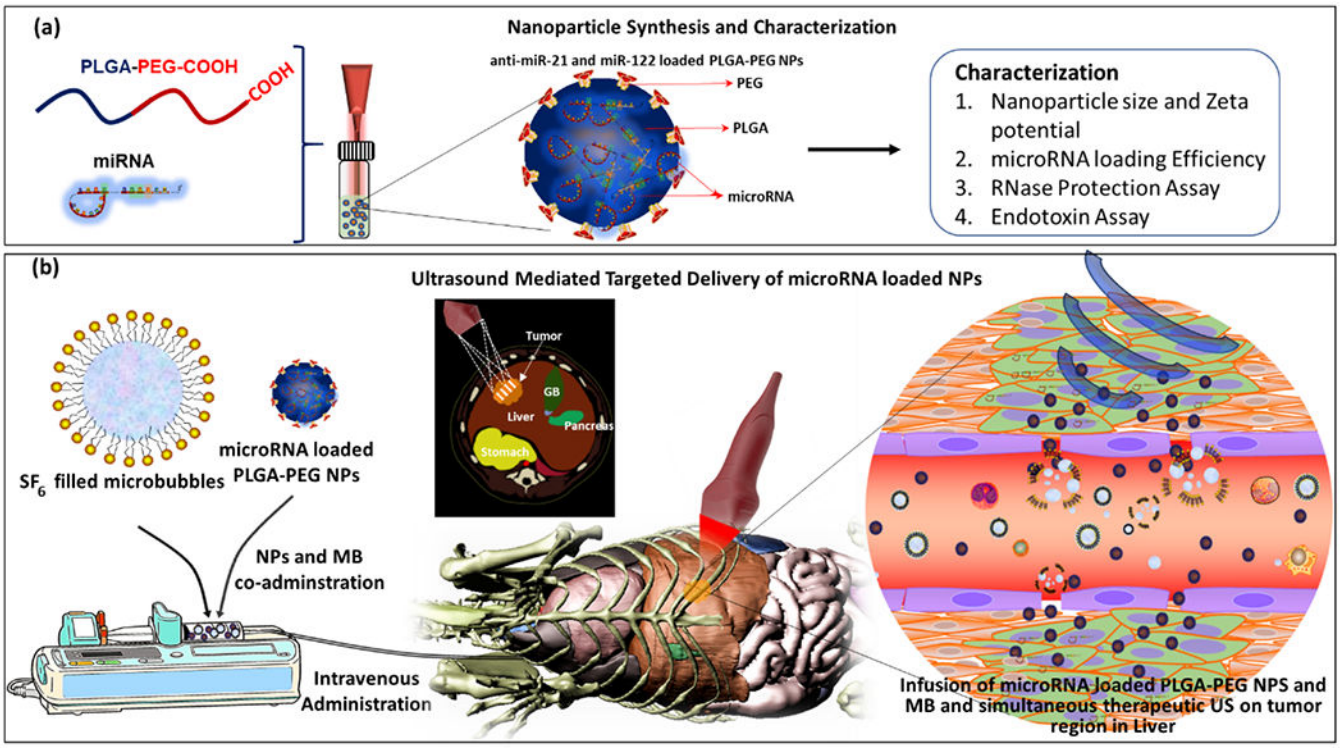

Figure 1. Overview of study.

Schematic outline of (A) microRNA-loaded PLGA-*b*-PEG nanoparticle synthesis and characterization, and (B) *in vivo* delivery by intravenous infusion of microbubbles and PLGA-*b*-PEG nanoparticles with an ultrasound transducer positioned on the tumor region for targeted microRNA delivery.

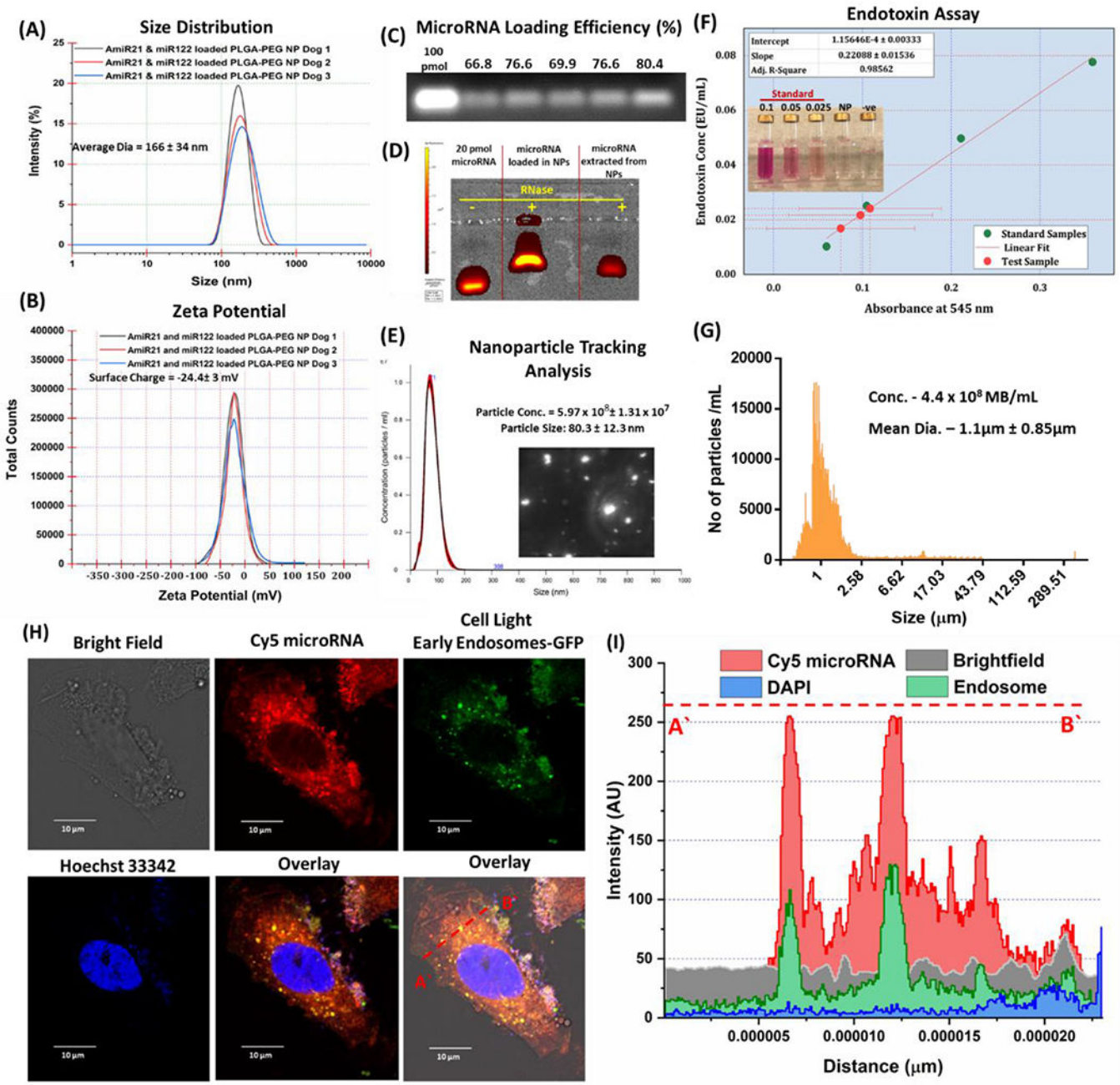

Figure 2. Characterization of microRNA loaded PLGA-*b*-PEG NPs and cellular uptake.

(A) size distribution and (B) zeta potential of microRNA-loaded PLGA-*b*-PEG nanoparticles; (C) microRNA-loading efficiency in PLGA-*b*-PEG nanoparticles; (D) RNase protection assay for microRNA-loaded in PLGA-*b*-PEG nanoparticles; (E) Concentration of PLGA-*b*-PEG nanoparticles estimated by Nanoparticle Tracking Analysis (Nanosight); (F) Endotoxin assay standard plot (green dots) with respect to microRNA-loaded PLGA-*b*-PEG NP **test samples (red dots);** (G) **Concentration and size distribution of** SonoVue microbubble contrast agent estimated by AccuSizer SPOS system; (H) Confocal microscopic images of microRNA-loaded PLGA-*b*-PEG NPs cellular uptake in HepG2 cells

stained with CellLight® Early Endosomes-GFP, BacMam 2.0 Marker and Hoechst 33342, under Bright field, Cy5, GFP, and DAPI filters. (I) Intensity line map over the region of interest (A‘----B‘) shows the intracellular microRNA in PLGA-*b*-PEG nanoparticles colocalized in endosomes. Data are shown as mean ± SD (n=3).

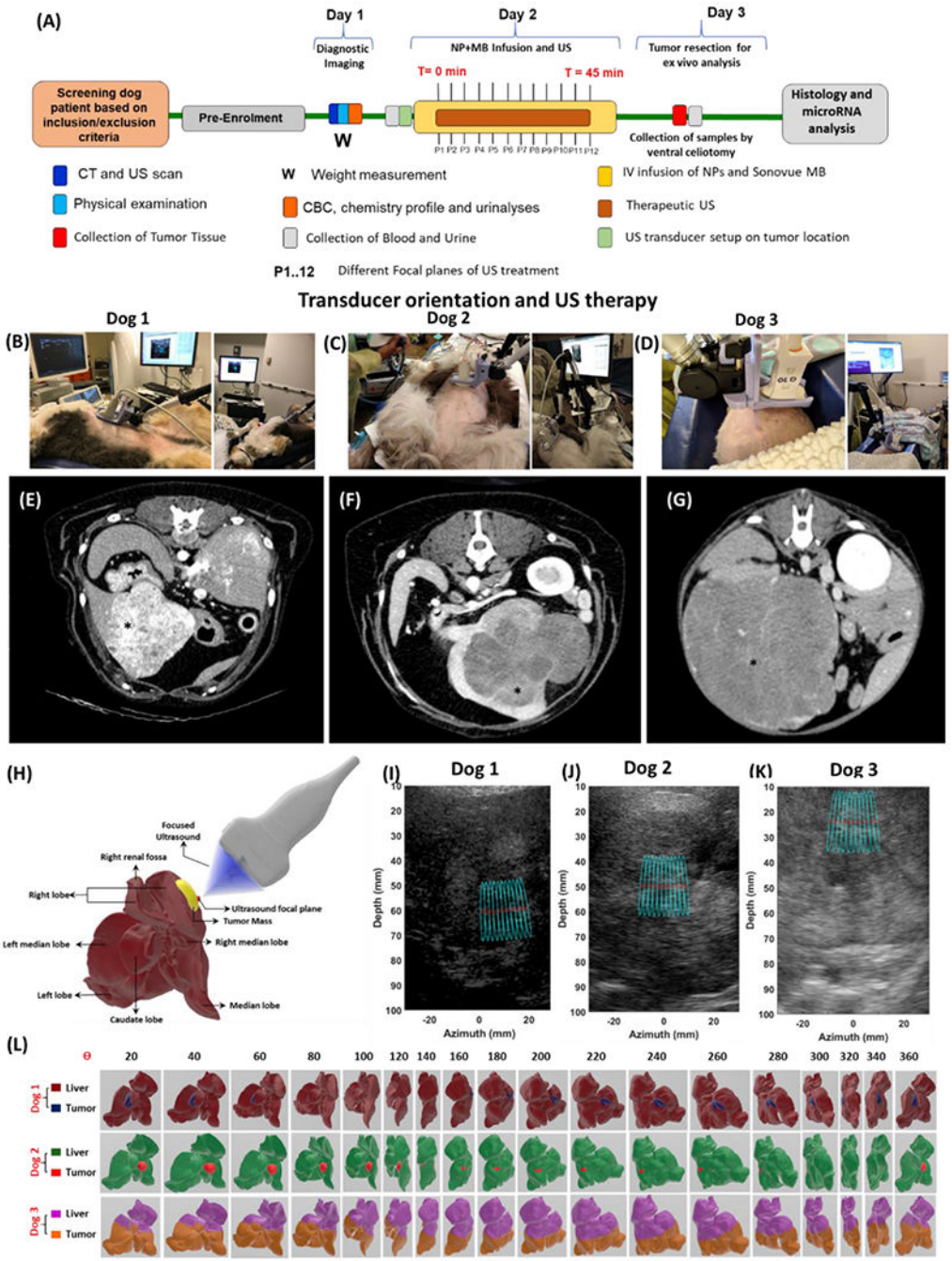

Figure 3. Timeline of procedure and evaluation of spontaneous hepatic neoplasia in dog patients.

(A) Schematic outline of complete timeline of procedures involved in the *in vivo* miRNA delivery study in dog model; (B-D) Ultrasound transducer setup and orientation for specific treatment region in the tumor of each dog patient; Contrast enhanced abdominal computed tomography (CT) images of dog 1 (E), and CT images of dog 2 (F), and dog 3 (G) showing the presence liver tumor mass with different sizes (* - tumor mass). (H) Schematic representation of dog liver anatomy and tumor mass for ultrasound guided microRNA delivery; (I-K) Abdominal ultrasound images of dog patients indicating the liver tumor and

region of ultrasound treatment; (L) 3D stereo view of liver lobes and tumor topology in each dog patient.

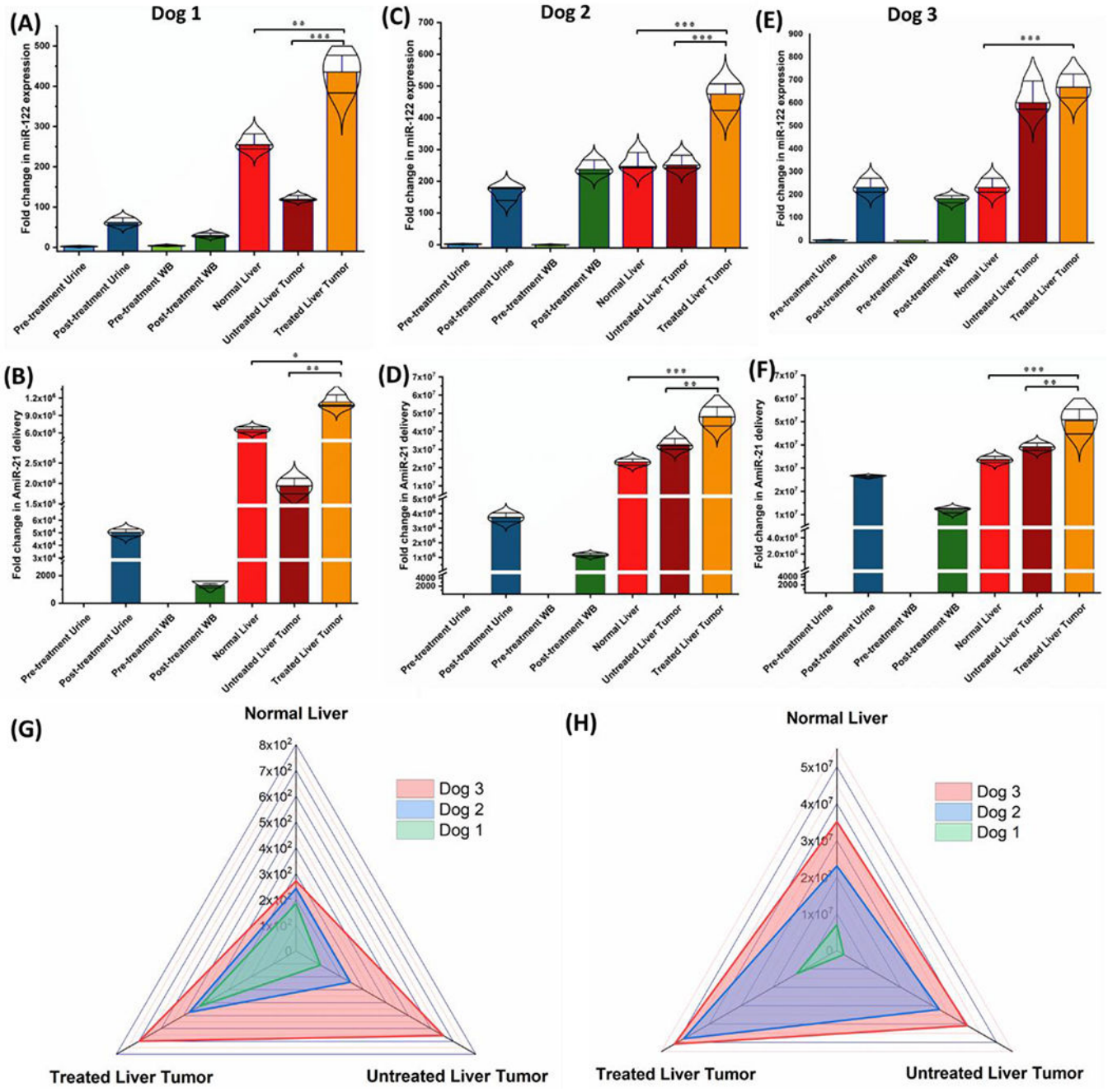

Figure 4. RT-PCR quantitation of delivered microRNA.

Quantitative RT-PCR analysis of miR-122 (A, C &E) and anti-miR-21 (B, D &F) in different tissues (normal liver, US treated tumor and untreated tumor), blood, and urine samples of dog patients (Dog 1 (A,B), Dog 2 (C,D) and Dog 3 (E,F)) received US-MB mediated delivery of miRNA loaded PLGA-*b*-PEG NPs (Violin plot with median, upper and lower quartiles); Comparative radar chart for (G) miR-122 and (H) anti-miR-21 and relative extent delivery in normal liver, treated liver tumor and untreated liver tumor in Dog 1, Dog 2 and Dog 3. Data are shown as mean ± SD (n=3).Unpaired, two tailed Student's t-test was used for comparison between two groups. *p≤ 0.05, **p≤ 0.001 and ***p≤ 0.0001

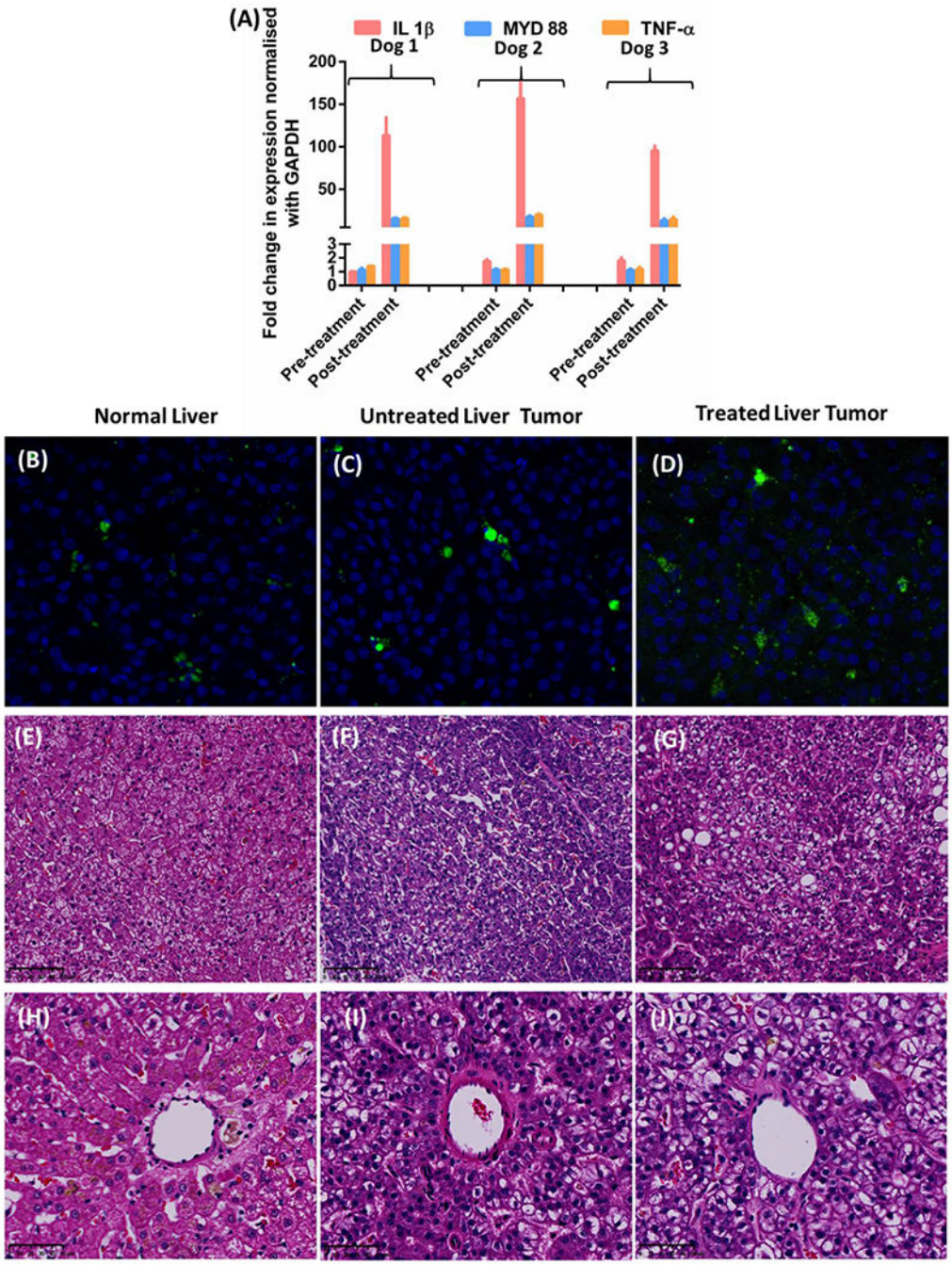

Figure 5. Inflammatory markers expression profile and tissue histopathology.

(A) Quantitative RT-PCR analysis of inflammatory cytokine markers in the blood of the dogs before and after ultrasound guided microRNA delivery (B-D) Immunohistology of CD8+ T cell population in normal liver, untreated liver tumor and US treated liver tumor region; H&E stained sections of (E, H) normal liver, (F, I) untreated liver tumor, and (G, J) US treated liver tumor tissue and associated blood vessel morphology. All data are shown as mean ± SD (n = 3).

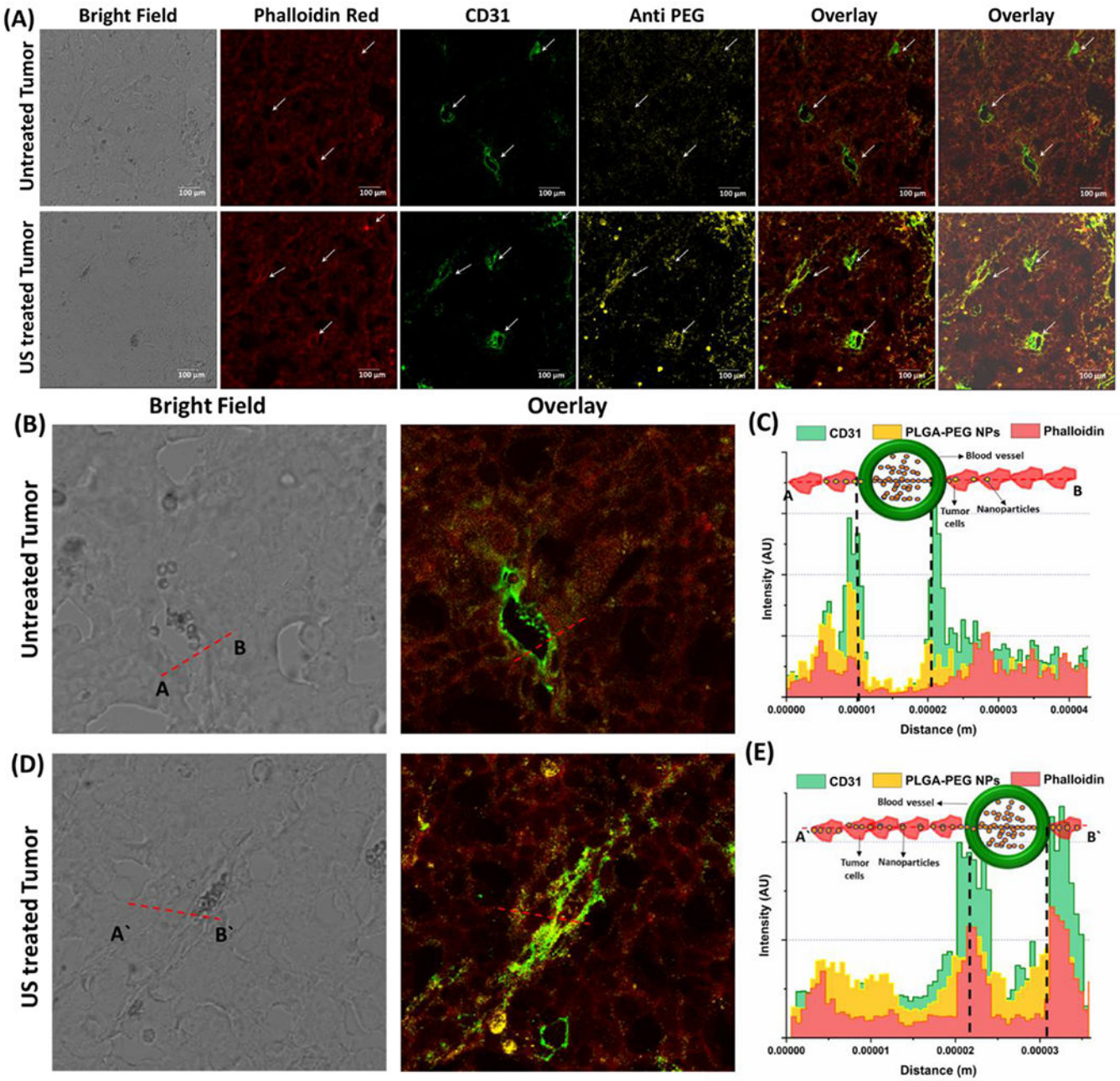

Figure 6. US-MB mediated delivery of PLGA-*b*-PEG NPs.

Confocal microscopic images of (A) untreated and US treated tumor tissues stained with Anti-PEG, anti-CD-31 and phalloidin (F-actin) red imaged under brightfield, Cy5 (633/670), FITC (488/525) and Phalloidin Red (514/609 nm) respectively; Magnified section of blood vessels in (B&C) untreated and (D&E) US treated tumor tissue showing NPs (Yellow color) permeation across the blood vessel (CD31-Green color) into extracellular space of tumor tissue and corresponding line intensity map of all three channels across the cross-section of blood vessel denoted by A----B and A‘-----B‘ segments.